



Ore-forming environment of Pb–Zn mineralization related to granite porphyry at Huangshaping skarn deposit, Nanling Range, South China

Da-peng ZHU¹, Huan LI¹, Wei-cheng JIANG², Chong WANG¹, Xiao-Jun HU¹, Hua KONG¹

1. Key Laboratory of Metallogenic Prediction of Nonferrous Metals and Geological Environment Monitoring, Ministry of Education, School of Geosciences and Info-Physics, Central South University, Changsha 410083, China;

2. Department of Earth and Environmental Sciences, Macquarie University, NSW, 2109, Australia

Received 7 August 2021; accepted 2 December 2021

Abstract: Multiple metallogenic types (skarn-type and vein-type) related to hypabyssal granites are found at the Huangshaping polymetallic deposit in the Nanling Range, South China. To constrain the crystallization and mineralization processes of skarn formation, three generations of magnetite and pyrrhotite from the hydrous silicate stage, oxide stage, early quartz–sulfide stage, and late quartz–sulfide stage were distinguished. The geochemical compositions of magnetite and pyrrhotite were obtained by electron probe microanalyzer (EPMA) and in-situ ablation–inductively coupled plasma–mass spectrometry (LA–ICP–MS). The results show that there may be silicate inclusions in magnetite and interaction of wall rock occurred in the mineralization process. The geochemical trends recorded in pyrrhotite show the influence of limestone during the crystallization of pyrrhotite. The re-equilibration temperatures of Po I, Po II, and Po III are 420.46, 380.45, and 341.81 °C, respectively, which suggests a continuous evolution following the high-temperature W–Sn mineralized system. The content change of Ni and V reflects a gradual decrease of oxygen fugacity from Mag I to Mag III, while the sulfur fugacity calculated from pyrrhotite gradually decreases. This continuous skarn mineralization evolution process helps us to better understand the change of metallogenic environment in the retrograde stage of the Huangshaping deposit.

Key words: trace elements; magnetite; pyrrhotite; geochemistry

1 Introduction

South Hunan hosts a major polymetallic mineralization district and is located in the western section of the Nanling metallogenic belt in South China. Complex tectonic activities accompanied by episodic magmatism occur at varying degrees and are at different stages in South Hunan. Among them, the Early Yanshanian activity is the most important, which is characterized by multiple stages of the magmatic activity and nonferrous metal mineralization [1], such as the Huangshaping, Shizhuyuan, Xianghualing, Furong, and Yaogangxian world-class endogenous polymetallic ore deposits

(Fig. 1) [2]. These polymetallic deposits are generally divided into two metallogenic systems: W–Sn–Mo–Bi and Pb–Zn–Ag–Cu [3]. The factors controlling the formation of these two mineralization systems include the geochemical composition of host rocks, faults and folds control, the emplacement depth of magmas, the intensity of deep-seated thermal perturbations, and the scale of magmatism of either I- or S-type granitoids [4–7]. The complex ore-forming process of these deposits, including skarn formation (especially less studied retrograde stage), is currently unclear. The metallogenic process and the metallogenic environment of the Pb–Zn stage are still uncertain, which hinders the complete understanding of the

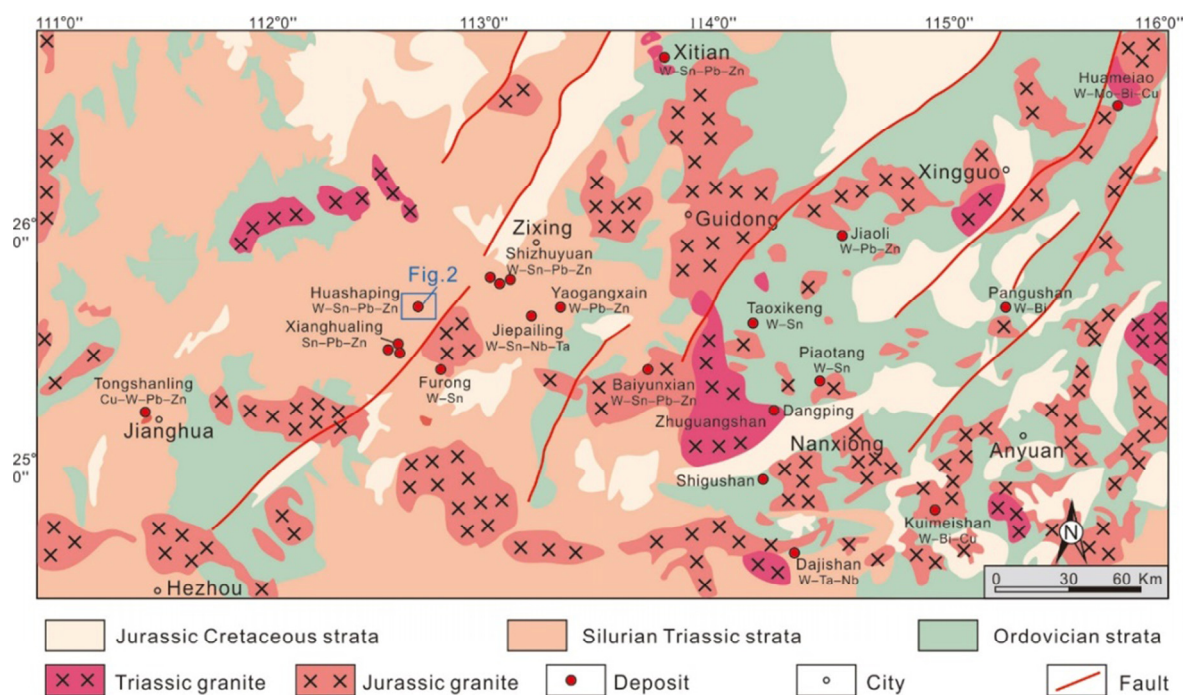


Fig. 1 Geology and distribution of major polymetallic deposits in Nanling Range, South China (modified from Ref. [2])

genesis of these skarn deposits.

The Huangshaping W–Mo–Pb–Zn polymetallic deposit, located in the southern part of Hunan Province, has been defined as an estimated resource of 22.43 Mt Pb–Zn at 3.60% Pb and 8.00% Zn, 74.31 Mt W–Mo at 0.28% WO_3 and 0.07% Mo, and 20.35 Mt Cu at 1.12% Cu [8]. The Huangshaping deposit is a typical skarn polymetallic deposit related to the magmatic-hydrothermal activities of the Late Jurassic granite porphyry and quartz porphyry intrusions [9–11]. The zircon U–Pb dating is mostly constrained between 160 and 150 Ma [4,12,13]. The results of the S, Pb, and Sr isotopes and whole-rock geochemistry show that the metals were derived from magmatic, Carboniferous wall rocks and underlying Paleoproterozoic basement end-members [4,13]. The superposition of different mineralization styles (skarn type, hydrothermal vein-type) makes the Huangshaping deposit a typical case for the study of W–Sn (Mo) and Pb–Zn composite mineralization. The prevailing view is that skarn W–Sn (Mo) and vein Pb–Zn ores at Huangshaping are belonging to a granite porphyry hydrothermal system and a quartz porphyry hydrothermal system based on the spatial–temporal association, respectively [4,8–11,14]. Although the Pb–Zn metallogenesis associated with quartz porphyry and

the W–Sn (Mo) metallogenesis were previously studied [4,8–15], the distal skarn Pb–Zn ore bodies associated with granite porphyry have received limited attention to date.

Magnetite is one of the most common oxide minerals of the spinel group, and its elemental composition varies physicochemically in mineral deposits. These variations have been used to characterize magnetite from different deposit types including skarn deposit, banded iron formation, and iron oxide–Cu–Au deposit [16,17]. Moreover, the compositions and properties (temperature, redox state, and degree of fluid–rock interactions) of the hydrothermal fluids can be derived from the trace element compositions and micro-inclusions of magnetite [16,18,19]. As a common accessory or ore mineral in skarn deposits, magnetite can record the temporal and spatial evolution of skarn systems based on the variations of trace elements from different stages [9,20,21]. Similarly, information about the hydrothermal fluids, such as temperature, sulfur fugacity, metal element migration, and precipitation can be derived from pyrrhotite, which is a common iron–sulfide accessory phase in the skarn system [22–24]. Recent advances in analytical techniques allow in-situ measurements of trace element concentrations in magnetite and pyrrhotite with sub-ppm detection limits by

LA-ICP-MS [25,26]. The chemical properties of magnetite and pyrrhotite, combined with detailed petrographic studies, are useful in fingerprinting and understanding the ore-forming processes and the evolution of hydrothermal fluids in skarn systems.

For this study, we present a multi-method, textural and morphological study (transmitted and reflected), major and trace element geochemistry of magnetite and pyrrhotite in skarn type ore bodies of the Huangshaping W–Sn–Pb–Zn deposit to establish the complete fluid evolution process of the retrograde stage and understand the metallogenic environment and the mechanism of mineral precipitation of the polymetallic mineralization.

2 Geological setting

2.1 Regional geology

The South China Block (SCB) is well known for its large-scale mineralization, which is among the important polymetallic metallogenic provinces in the world. The northwest Yangtze Block and the southeast Cathaysia Block along the Jiangnan Orogen formed the South China Block by the collision of two blocks during the Neoproterozoic (860–780 Ma) [27]. The Jiangshan–Shaoxin Fault and the Chenzhou–Linwu Fault are the structures separating these two blocks. The South Hunan is characterized by complex geological conditions and rich mineral resources in the central Nanling Region with a large number of nonferrous metal elements (e.g., W, Sn, Mo, Bi, Cu, Zn, Pb, and Sb) and high mineral concentrations [28].

The Nanling region, an important W–Sn–Mo–Bi–Pb–Zn metallogenic belt, is located in the northwestern part of the Cathaysian Block (Fig. 1). The sedimentary strata of the Nanling Range consist of a basement comprising Sinian to Ordovician clastic rocks, the Devonian to Triassic carbonate, marlstone, and clastic rocks, and the Jurassic to Cretaceous clastic rocks, volcanic rocks, and red beds [2]. Complex thermo-tectonic events developed in the Nanling region in different stages during the Early Paleozoic (~450 Ma), the Triassic (~240 Ma), and the Jurassic (~160 Ma) [29]. As a result, Late Mesozoic granites are distributed in most areas of the Nanling Range and the Early Triassic (Indosinian) granites occur in the Zhuguangshan mountains (Fig. 1) [2,30]. The

Sinian (Precambrian)–Cambrian sedimentary rocks have experienced strong metamorphism since the Caledonian (Cambrian–Silurian), resulting in an EW-striking tight fold and EW- and NE-trending faults in the regional basement. The majority of the deposits are hosted in the Late Paleozoic sediments consisting of Devonian and Permian carbonate strata.

The fracturing of the Paleo-Pacific Plate and the Early Yanshanian movement (~190–140 Ma) played a significant role in the formation of multiple stages of intrusions and associated abundant polymetallic ore deposits, which are distributed along the NNE-trending Chenzhou–Linwu deep-seated fault zone [8,31,32]. Two metallogenic systems can be distinguished: W–Sn–Mo–Bi mineralization in the southwest and Pb–Zn–Cu–Ag mineralization in the northwest [8]. In fact, these two metallogenic systems coexist in several deposits in the Nanling Range, including the Xianghualing Sn–Pb–Zn deposit, the Huangshaping W–Sn–Pb–Zn deposit, the Shizhuyuan W–Sn–Pb–Zn deposit, the Xitian Sn–Pb–Zn deposit, the Yaogangxian W–Sn–Pb–Zn deposit, and the Furong W–Sn deposit (Fig. 1) [7,11,33,34].

2.2 Geology of Huangshaping deposit

The large Huangshaping W–Sn–Pb–Zn polymetallic deposit is located in the southern part of the Hunan Province, the central Nanling Range. It is a representative skarn type deposit genetically related to Jurassic magmatism. It has been mined as a Pb–Zn deposit since 1967. Several W–Sn and Cu ore bodies were successively discovered beneath the Pb–Zn ore bodies at deep levels. The deposit is genetically associated with Late Jurassic granitic plutons and has large reserves of WO_3 (152.9 kt), Sn (38.2 kt), Pb (761.3 kt), and Zn (1.5291 Mt) [15]. The Huangshaping deposit occurs in a series of sedimentary rocks, including neritic marine sediment of the Upper Devonian Xikuangshan Formation limestone, the Lower Carboniferous Donglingao Formation limestone, the Zimenqiao Formation dolomite and limestone, the Shidengzi Formation limestone, the Shetianqiao Formation limestone, and the Ceshui Formation sandstone (Fig. 2(a)) [12]. The Shidengzi Formation limestone is the most favorable host for W–Sn–Pb–Zn mineralization, followed by minor mineralization in the Ceshui Formation sandstone (Figs. 2(b, c)) [4,35].

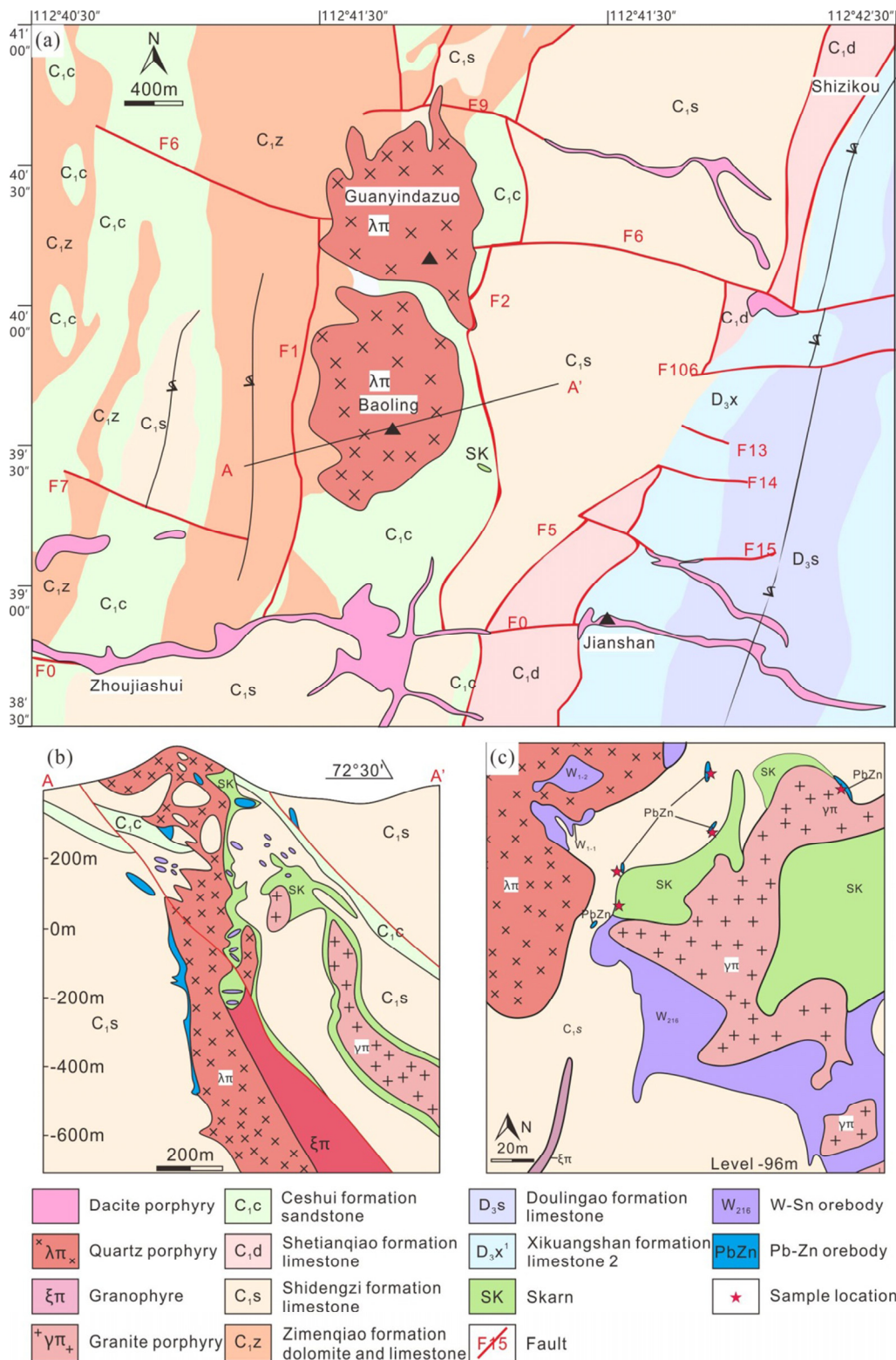


Fig. 2 Geological map of Huangshaping polymetallic deposit (a) (modified from Ref. [12]), vertical geological profile of No. 16 prospecting line (b) (modified from Ref. [4]), and simplified geological map of Huangshaping deposit at -96 m level (c) (modified from Ref. [35])

The tectonic structures in the Huangshaping deposit comprise numerous folds and faults, developed from Triassic to Jurassic [13]. The

dominant structure is the NS-trending Guanyindazuo–Baoling reverse anticline, which contains the Shidengzi Formation in its core while

the limbs comprise the Ceshui and Zimenqiao Formations (Fig. 2(a)). Three NS-trending thrust faults (F1, F2, F3) control most of the W–Sn–Pb–Zn reserves, which are present within the Guanyindazuo–Baoling anticline ores and limbs (Fig. 2(b)). Several EW-trending normal faults (F0, F6, F7, F9) occur within the deposit. These anticlines and faults jointly formed a “#”-shaped structural pattern that controlled the distribution of the granite intrusions and W–Sn–Pb–Zn mineralization [10].

The granite intrusions of the study area include outcropping quartz porphyry and dacite porphyry, as well as the subsurface granophyre and granite porphyry, all of which belong to the Late Jurassic felsic intrusions (Fig. 2). The quartz porphyry contains feldspar and quartz as phenocrysts within a felsitic groundmass forming two mountain peaks known as Baoling and Guanyindazuo (Fig. 2(a)). In contrast, the dacite porphyry formed as dykes or stocks with dozens of small granitoids along EW trending faults to the south of the quartz porphyry (Fig. 2(a)). It mainly consists of alkali feldspar, quartz, minor biotite, amphibole, and pyrite. The granophyre and granite porphyry are distributed in the southeast and west of the mining district, respectively (Fig. 2(b)). The granophyre has a granophyric texture with 8%–15% phenocrysts of alkali feldspar (50%–60%) and quartz (35%–40%) in a granophyric groundmass. The granite porphyry shares similar mineral assemblages and whole-rock geochemical compositions with granophyre, which has a porphyritic or glomerophyric texture and contains phenocrysts of quartz, alkali feldspar, and minor amounts of plagioclase, with fine-grained quartz and feldspar as the groundmass. LA–ICP–MS zircon U–Pb dating suggests that the crystallization ages of the quartz porphyry, granophyre, and granite porphyry are 160–155, 157–150, and 155–150 Ma, respectively [7]. The granophyre and granite porphyry are suggested to be sourced from the same magma batch but experienced different degrees of fractional crystallization at depth [36].

The Huangshaping deposit yields numerous kinds of metallic mineralization, including Pb, Zn, W, Mo, Cu, Fe, and a lesser amount of Bi, Sn, and Ag. Hundreds of veined, lenticular, and irregular orebodies have been discovered in the Huangshaping deposit, with a length of 200–400 m

and a width of 4–10 m. As the primary alteration type in the Huangshaping deposit, skarn alteration is outward from proximal garnet-diopside skarn to distal garnet-vesuvianite-tremolite skarn genetically associated with granite porphyry, while from proximal garnet-diopside skarn to distal garnet skarn genetically related to quartz porphyry [37]. Skarn-type and hydrothermal vein-type polymetallic mineralization were classified according to the mineral association and occurrence. The skarn-type mineralization mainly occurs in the No.W₂₁₆ and No.W₁ polymetallic ore clusters. The No.W₂₁₆ is situated in the contact zone of the granite porphyry and limestone, which is characterized by typical calc-silicate skarn associated with W, Mo, Pb, Zn, Fe, and Sn mineralization. The No.W₁ develops around the quartz porphyry, accompanied by relatively few amounts of skarns. Based on the stable isotope and fluid inclusion studies, the W–Sn (Mo) mineralization formed at temperatures of >400 °C, while Pb–Zn mineralization formed at lower temperatures of 200–300 °C [8]. The latest research [38] indicated that associations of Pb–Zn mineralization with quartz porphyry and W–Sn (Mo) mineralization with granite porphyry according to the relationships between metallogenic elements and their host rocks. In addition, the metal sources of mineralization were considered to come mainly from granite and sedimentary, respectively [4,9,10]. On this basis, the W–Sn (Mo) mineralization is related to granite porphyry, while Pb–Zn mineralization is related to quartz porphyry, considering geochronology, ore type, temperature, and metal source [12,14,39]. Exceptionally, small-scale Pb–Zn mineralization studied in this work develops in the distal skarn within the Shidengzi Formation spatially associated with W–Sn (Mo) mineralization in the proximal skarn (Fig. 2(c)). The skarn minerals are dominated by diopside, actinolite, garnet, chlorite, and epidote, and ore minerals mainly consist of scheelite, molybdenite, magnetite, pyrrhotite, arsenopyrite, pyrite, chalcopyrite, sphalerite, and galena. The hydrothermal vein-type mineralization develops in the fractures and joints of the limestones away from the quartz porphyry. Variable amounts of sphalerite, galena, pyrrhotite, chalcopyrite, arsenopyrite, quartz, and calcite are the main minerals in the hydrothermal vein-type ore bodies.

The No.W₂₁₆ skarn ore bodies, associated with W, Mo, Pb, Zn, Fe, and Sn, are zoned outward from the proximal garnet–diopside skarn to the distal tremolite–actinolite skarn [9,15]. A detailed paragenetic sequence of the mineralization with five stages of skarn (anhydrous silicate stage, hydrous silicate stage, oxide stage, early quartz–sulfide stage, and late quartz–sulfide stage) has been proposed by previous researches [8–10,13]. Andradite, grossularite, and diopside are the principal minerals of the anhydrous silicate stage (Figs. 3(a) and 4(a, b)), followed by tremolite, actinolite, and epidote in the hydrous silicate stage. In the oxide stage, the main mineral phases are magnetite, quartz, molybdenite, and minor cassiterite. Pyrite, chalcopyrite, and pyrrhotite are typical minerals of the early quartz–sulfide stage (Figs. 3(b–f) and 4(b–d)), while sphalerite and galena precipitated in the late quartz–sulfide stage (Figs. 3(g–i) and 4(e–i)). Quartz, chlorite, and epidote are the main gangue minerals present in the quartz–sulfide stage (Figs. 4(c, f)). The paragenetic sequence of mineralization for the Huangshaping

deposit is illustrated in Fig. 5.

3 Samples and analytical methods

3.1 Samples

Five representative samples analyzed in this study were collected from the distal skarn around the No.W₂₁₆ ore body in a mining tunnel at the –96 m level of the Huangshaping deposit (Fig. 2(b)). This mining tunnel shows the retrograde stage of the skarn mineralization. Sample HSP-1 was collected from the altered garnet–magnetite skarn, sample HSP-2 from the actinolite–quartz–magnetite skarn, sample HSP-3 from quartz–epidote–magnetite–pyrite–pyrrhotite skarn. Samples HSP-4 and HSP-5 are sulfide ores, and their respective mineral assemblages are pyrrhotite–pyrite–arsenopyrite–quartz and pyrrhotite–pyrite–sphalerite–galena, respectively.

3.2 Analytical methods

In-situ major element analyses of the pyrrhotite were performed at the Key Laboratory of

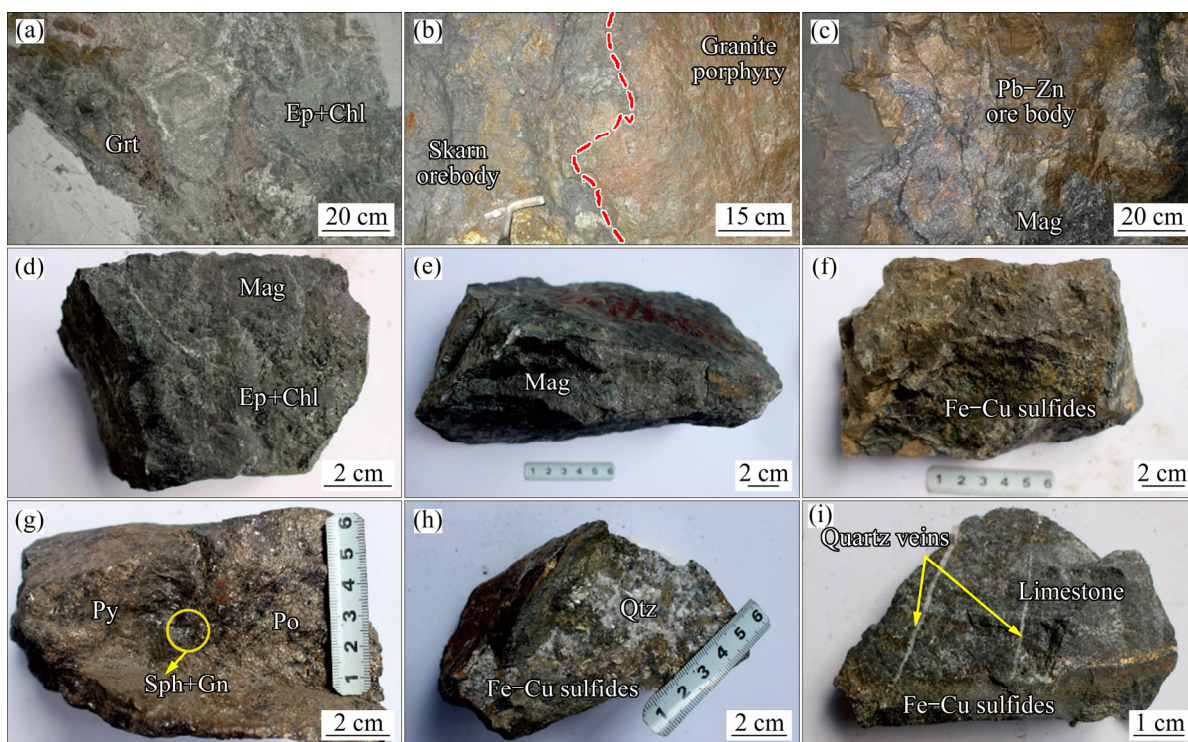


Fig. 3 Field and hand specimen photos of skarn and ore bodies: (a) Garnet–chlorite–epidote skarn; (b) Relationship between skarn orebody and granite porphyry; (c) Pb–Zn ore body; (d) Magnetite–chlorite–epidote skarn; (e) Massive magnetite; (f) Disseminated ores with chlorite–epidote alteration; (g) Sample of meter-scale massive Fe–Cu–Zn mineralization; (h) Fe–Cu mineralization accompanied by quartz; (i) Boundary between limestone and Fe–Cu sulfides, accompanied by calcite veins (Chl–chlorite; Ep–epidote; Grt–garnet; Gn–galena; Mag–magnetite; Po–pyrrhotite; Py–pyrite; Qtz–quartz; Sph–sphalerite)

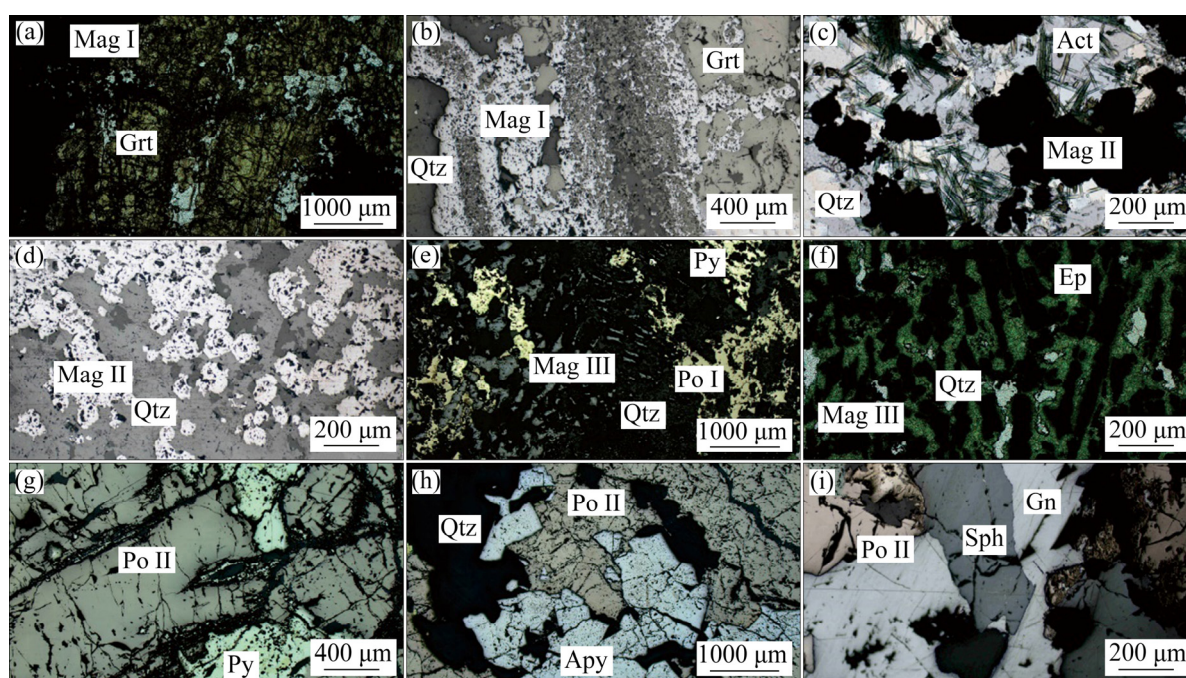


Fig. 4 Photomicrographs of typical samples in the Huangshaping deposit: (a, b) Early garnet altered to magnetite (Mag I) and quartz; (c, d) Magnetite associated with quartz and actinolite (Mag II); (e, f) Magnetite associated with quartz, pyrrhotite, and epidote (Directional distribution of magnetite and epidote (Mag III and Po I)); (g, h) Pyrrhotite associated with pyrite and arsenopyrite (Po II); (i) Pyrrhotite associated with sphalerite and galena (Po III) (Act–actinolite; Apy–arsenopyrite; Ep–epidote; Grt–garnet; Gn–galena; Mag–magnetite; Po–pyrrhotite; Py–pyrite;)

Metallogenic Prediction of Nonferrous Metals, Central South University (Changsha, China) using an electron probe microanalyzer (EPMA–170/1720H). The spot analysis experimental conditions were 15 kV accelerating voltage, 10 nA electron beam current, and 5 μm electron beam diameter. The following nine elements were analyzed: As (K_{α}), W (M_{α}), Fe (K_{α}), Mo (M_{α}), Co (K_{α}), S (K_{α}), Cu (K_{α}), Pb (M_{α}), and Zn (K_{α}). The typical detection limits of these elements are about 0.01%. Analysis data were processed using the Shimadzu software.

Trace element analyses of magnetite and pyrrhotite were conducted at the Sample Solution Analytical Technology Co., Ltd, (Wuhan, China) using the LA–ICP–MS. Laser sampling was performed using a GeoLas 2005. An Agilent 7500a ICP–MS instrument was used to acquire ion–signal intensities. The He carrier gas and make-up Ar gas are mixed through a T-shaped joint before entering the ICP. A small amount of N is added to the plasma center gas flow (Ar + He) to increase the sensitivity of the instrument, and reduce the

detection limit and improve the precision of the analysis [40]. A “wire” signal smoothing device is included in this laser ablation system, by which smooth signals are produced even at very low laser repetition rates down to 1 Hz [41]. Each time-resolved analysis includes 20–30 s blank and 50 s sample signal. Spot analysis of magnetite and pyrrhotite was run with a laser-ablating spot of 44 μm pit size, 10 Hz pulse frequency, and 5 J/cm^2 fluences. Pyrrhotite was used to calibrate the concentration of S. NIST–610 was used to calibrate and convert the integrated count data to concentration for other elements. MASS-1 as sulfide reference materials was analyzed as unknown to check the analytical accuracy. Element content was calibrated against multiple-reference materials (BCR–2G, BIR–1G, and BHVO–2G) without applying internal standardization for magnetite [42]. The data processing (including the selection of samples and blank signals, correction of instrument sensitivity drift, calculation of element content) was completed using the software ICPMSDataCal [42].

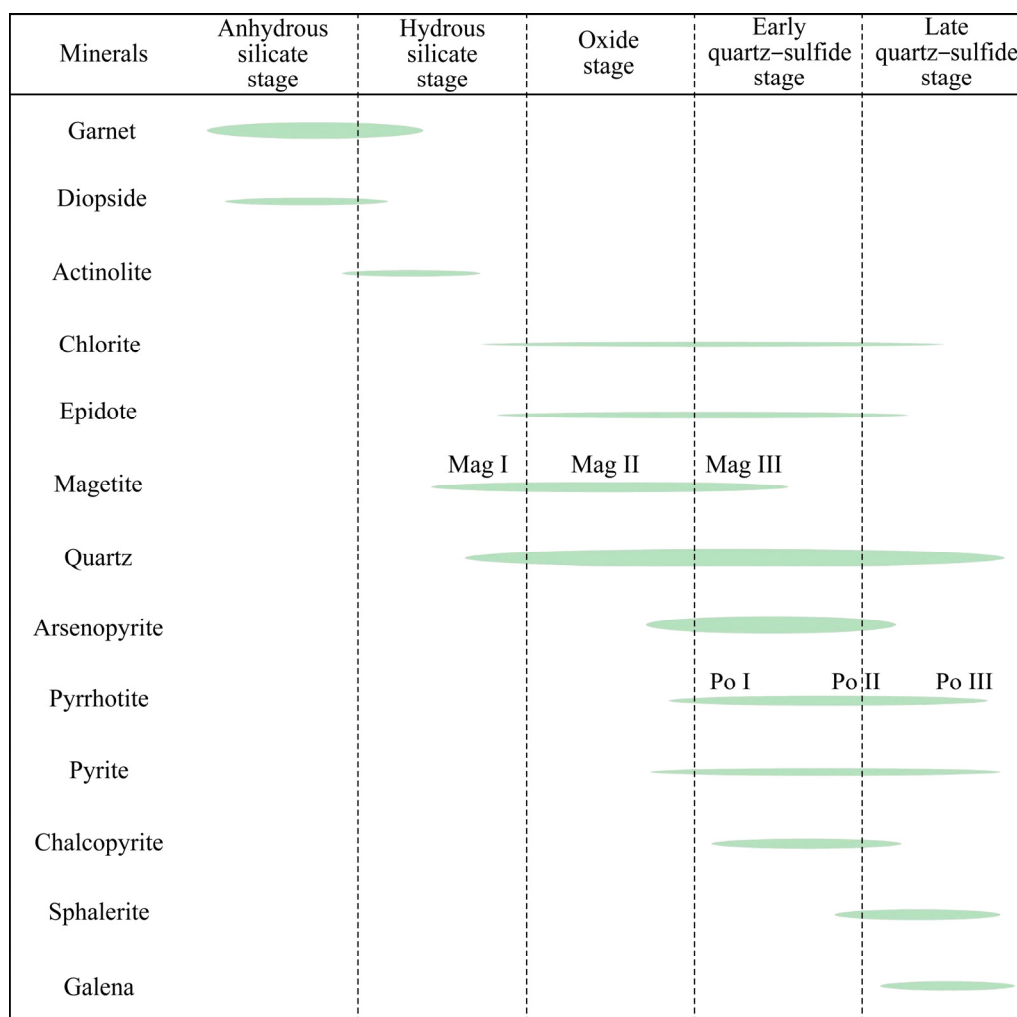


Fig. 5 Paragenetic sequence of mineral growth in Huangshaping deposit (Line widths indicate relative mineral abundance)

4 Results

4.1 Ore petrography

The distal skarn Pb–Zn ore bodies associated with the granite porphyry are both massive and disseminated ores with highly variable amounts of pyrite, magnetite, pyrrhotite, sphalerite, and galena. Magnetite and pyrrhotite occurred in multiple stages of skarn mineralization.

Three types of magnetite are identified in the studied samples based on textural relationships and associated minerals. The texturally earliest magnetite (Mag I) is volumetrically minor to medium and occurs in veinlets with quartz, replacing garnet (Figs. 4(a, b)). Patchy alteration and recrystallization of the garnet intergrowth produced coarser patches of Mag I, which can be

recognized as the earliest magnetite and formed after the prograde stage. Magnetite formed at the oxide stage (Mag II) is usually medium-coarse grained (100–300 μm), and subhedral to euhedral, associated with quartz and actinolite (Figs. 4(c, d)). Mag II shows octahedron shapes, typical for spinel group minerals (Fig. 4(d)). By contrast, Mag III is volumetrically minor and forms elongated crystals, associated with epidote, a small amount of quartz, and sulfides (such as pyrite and pyrrhotite: Po I) (Figs. 4(e, f)).

Similar to magnetite, pyrrhotite is also found in different mineralization stages. The earliest pyrrhotite (Po I) precipitated with Mag III during the early quartz–sulfide stage and shows disseminated, small and anhedral grains (Fig. 4(e)). Pyrite, arsenopyrite and quartz are the main associated minerals of pyrrhotite II (Po II), which is

an important sulfide in the quartz–sulfide stage. Po II is coarse-grained and euhedral (Figs. 4(g, h)). In the late quartz–sulfide stage sphalerite and galena are accompanied by small amounts of pyrrhotite (Po III) and pyrite.

In summary, field and petrographic observations suggest that skarn mineralization involves multiple stages. This study mainly focuses on the mineral evolution of each sub-stage in the retrograde stage, which ranges from the hydrous silicate stage to the late quartz–sulfide stage.

4.2 Major element compositions of pyrrhotite

The major element compositions of the three generations of pyrrhotite in the Huangshaping deposit are given in Table S1 of the supplementary materials. The stoichiometric values of Fe and S in troilite are 63.53 wt.% and 36.47 wt.%, respectively. The average values of Fe and S of pyrrhotite in the Huangshaping deposit are 59.76 wt.% and 38.28 wt.%, respectively. The contents of Fe and S in pyrrhotite (Po I) associated with magnetite are 58.85–60.24 wt.% and 37.97–38.85 wt.%, respectively, with an average of 59.66 wt.% and 38.42 wt.%. Po II and Po III contain fairly uniform Fe (58.78–60.05 wt.% and 58.97–60.83 wt.%) and S (37.48–38.95 wt.% and 37.44–38.82 wt.%). The average content of Fe atoms from Po I to Po III is 46.88%, 48.00%, and 47.16%, respectively, while the average content of S atoms is 52.60%, 53.02% and 52.32%, respectively.

4.3 Trace element composition of magnetite and pyrrhotite

Four representative magnetite grains in three generations were selected for trace element analyses for a total of forty spots (Mag I: $n=19$; Mag II: $n=15$; Mag III: $n=6$; Table S2 of the supplementary materials). Similarly, a total of thirty-five spot analyses for the three generations of pyrrhotite (Po I: $n=13$; Po II: $n=8$; Po III: $n=13$; Table S3 of the supplementary materials) were carried out.

The trace element compositions of the different generations of the Huangshaping magnetite vary. Elements such as Na, Al, K and Ca show a decreasing trend from Mag I to Mag II followed by an increase of content in Mag III (Fig. 6(a)). Si content increases gradually from Mag I to Mag III, while Ti shows the opposite trend and the lowest

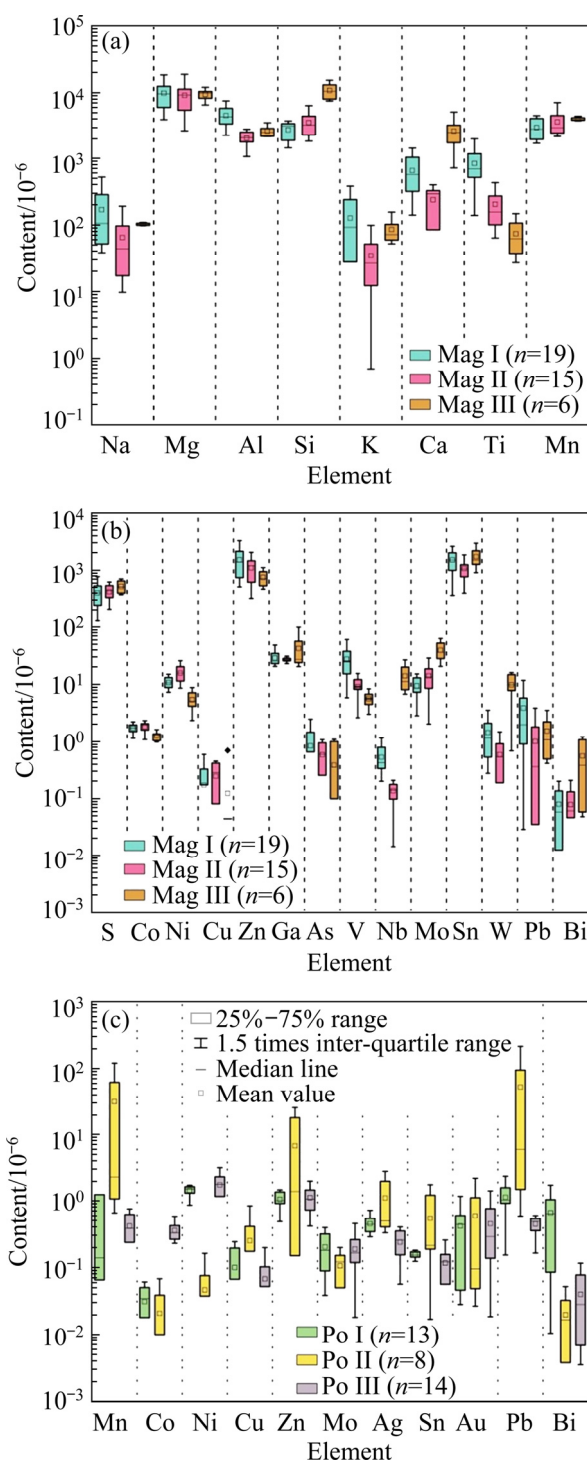


Fig. 6 Box chart for lithophile elements in magnetite (a), chalcophile and siderophile elements in magnetite (b) and in pyrrhotite (c)

content in Mag III ($(139-1976) \times 10^{-6}$ in Mag I, $(64-433) \times 10^{-6}$ in Mag II, and $(27-148) \times 10^{-6}$ in Mag III). Mg and Mn do not show discernable trends among the three generations of magnetite (Fig. 6(a)). A variety of trends also exist in the metallic elements, where notably Zn and Sn show

the highest concentrations for all generations (Fig. 6(b)). Their content is more than 1000×10^{-6} . The average Zn content is as follows: Mag I: 1501×10^{-6} , Mag II: 1290×10^{-6} , Mag III: 750×10^{-6} , and for Sn it is Mag I: 1481×10^{-6} , Mag II: 1070×10^{-6} , and Mag III: 1729×10^{-6} . Furthermore, Mag I shows the highest Pb and As content among the three generations. The youngest magnetite generation (Mag III) is characterized by the highest Nb, W, Mo, and Bi content (Fig. 6(b)). Magnetite II is slightly enriched in Ni, but somewhat depleted in Nb, Sn, and W compared to the other two magnetite generations. V shows a comparable trend to Ti, although with very much lower absolute content. V is the highest in Mag I ($(6-86) \times 10^{-6}$, mean 32×10^{-6}) and the lowest in Mag III ($(3-9) \times 10^{-6}$, mean 6×10^{-6}). In the binary correlation diagram, with Si as the abscissa, Si shows an evident positive correlation with Na, Mg, K and Ca (Fig. 7).

The contents of chalcophile elements (Cu, Zn,

Ag, Pb, and Bi), and siderophile elements (Co, Ni, and Sn), Mn, Mo, and Au are higher than the detection limit in pyrrhotite and can be used as discrimination elements for this mineral. Other elements (Rb, Sr, Zr, Nb, Ta, and REE) are below or near the detection limit and are not listed in Table S3 of the supplementary materials. In general, the trace element content in pyrrhotite from Huangshaping is very low (typically $<10 \times 10^{-6}$). Elements that are most enriched are Mn, Cu, Zn, Ag, Sn, and Pb, and they all occur in Po II. This generation of pyrrhotite is nevertheless depleted in Ni (and to some degree in Co, Mo, Bi). Po III is depleted in Pb and Ag. The first generation pyrrhotite (Po I) is elevated in Bi, while the latest generation (Po III) is enriched in Ni ($(1.08-3.18) \times 10^{-6}$) and Co ($(0.23-0.58) \times 10^{-6}$) compared to the other generations (Fig. 6(c)). These two elements distinguish the three generations of pyrrhotite best (Fig. 8(a)), and in general, it is Po II that is different compared to the other two generations (Fig. 8).

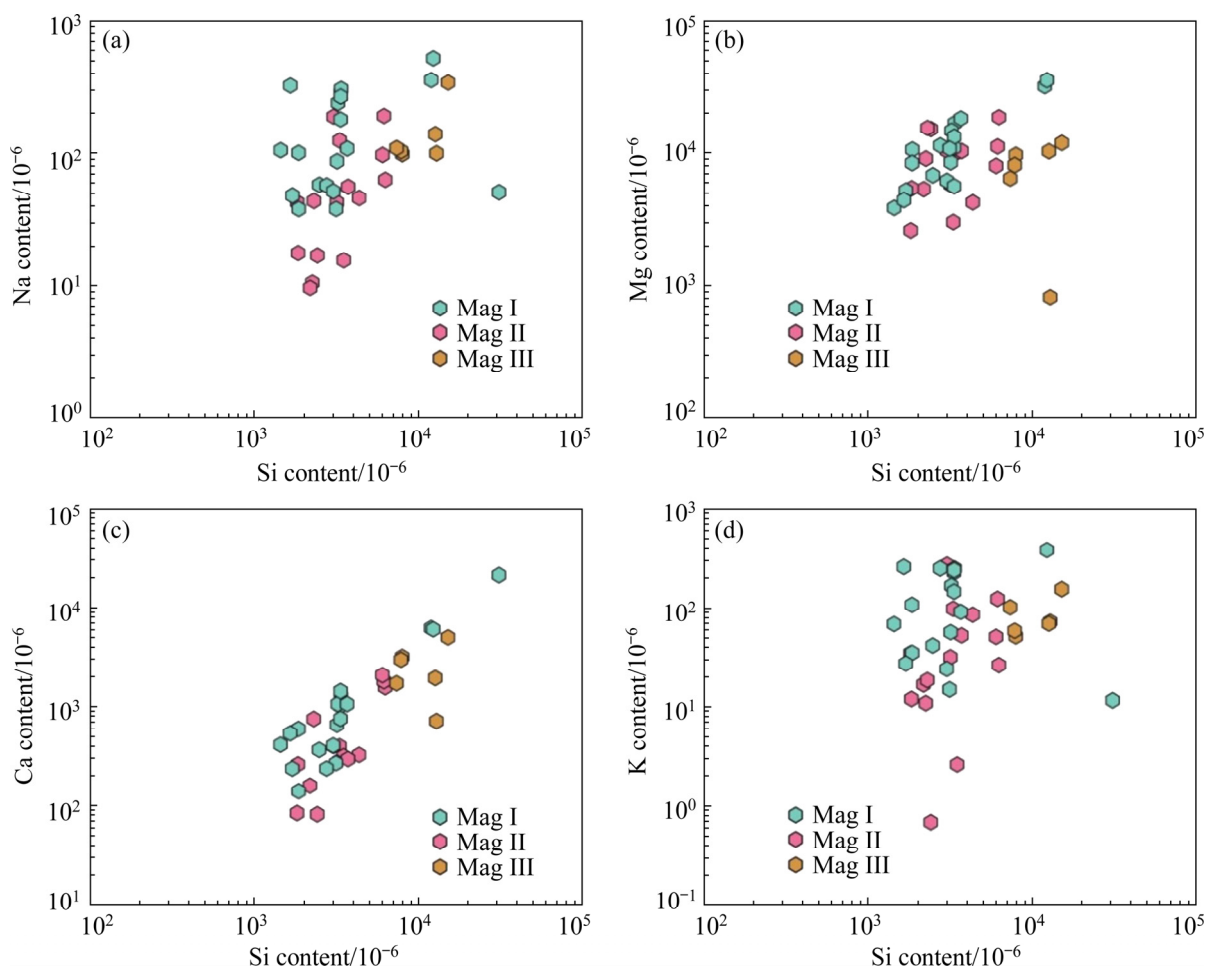


Fig. 7 Scatter diagrams of selected elements in magnetite: (a) Si vs Na; (b) Si vs Mg; (c) Si vs Ca; (d) Si vs K

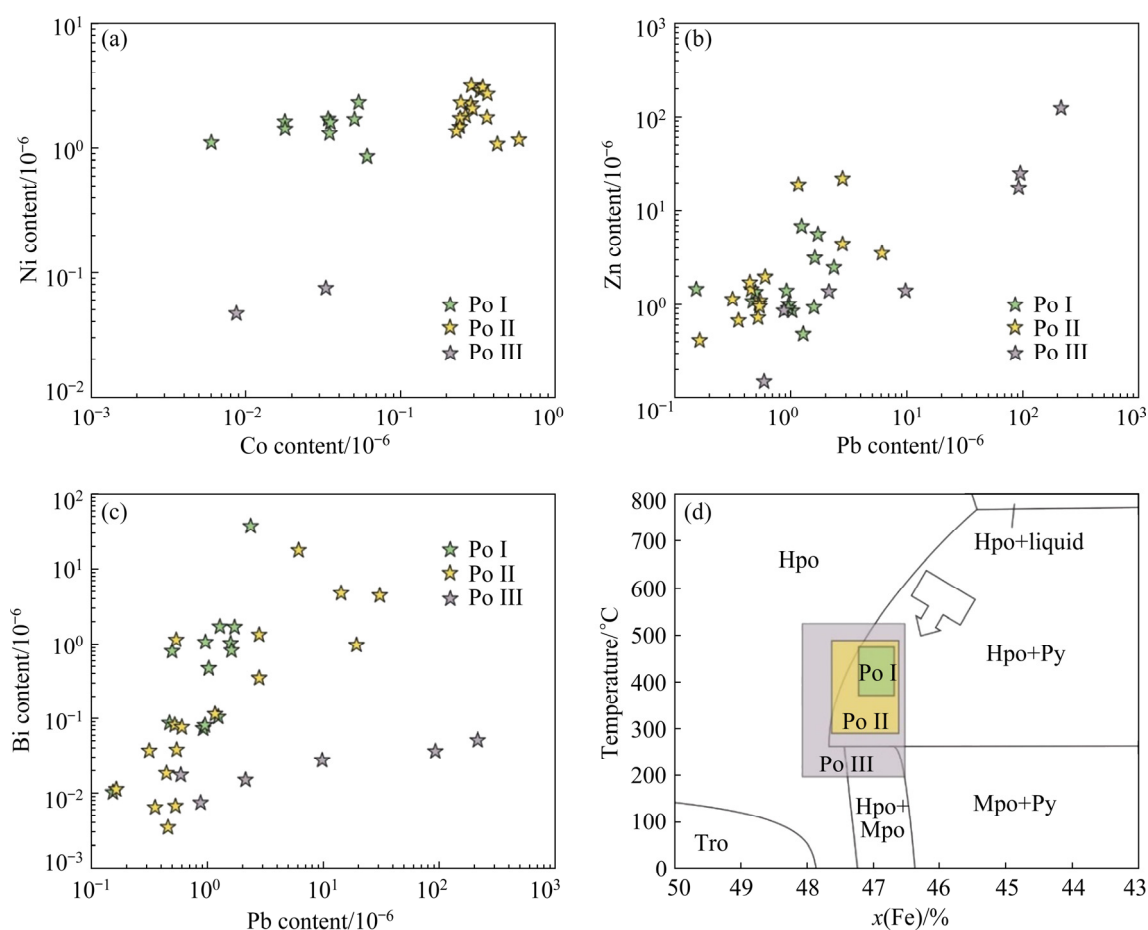


Fig. 8 Scatter diagrams of trace elements in pyrrhotite: (a) Co vs Ni; (b) Pb vs Zn; (c) Pb vs Bi; (d) Equilibrium diagram of Fe–S mineral phase system [43–46]

5 Discussion

5.1 Trace element speciation in magnetite and pyrrhotite

Magnetite has an inverse spinel structure and is described by the general formula XY_2O_4 , where X represents divalent cations, such as Fe^{2+} , Mn^{2+} , Mg^{2+} , Zn^{2+} , Ni^{2+} or Co^{2+} , and Y represents a trivalent cation, such as Fe^{3+} , Al^{3+} , Cr^{3+} , V^{3+} , Mn^{3+} or Ga^{3+} , or represents tetravalent cations such as Ti^{4+} or Sn^{4+} by coupling the substitution with the divalent cation [47,48]. These elements have a stable time-resolved LA–ICP–MS signal without any clear peaks in magnetite from the Huangshaping deposit (Fig. 9(a)).

Ca, K, Na and Si are usually below detection limits in magnetite unless they occur as mineral inclusions, which can represent relics of early gangue minerals [49]. Sulfide inclusions and silicate inclusions, not exposed on the sample surface, can be identified from the time-resolved

analytical signals of LA–ICP–MS analyses, which may be indicated by synchronous and sporadic increases in Cu, Co, Sn, S and K, Mg, Al, Si, respectively [18,49]. The time-resolved analytical signals of magnetite reveal that some alkali metal elements (e.g., Na, K, and Ca) have high-intensity signals. Except for Al, Ca, Mg and Na show positive correlations with Si in the magnetite, indicating that a small proportion of Mg, Ca and Na can enter magnetite as silicate inclusions [48].

Based on the calculated temperature data (discussed in Section 5.2.1), in the pyrrhotite phase diagram, Po I and Po II fall into both the Hpo and Hpo + Py regions, while Po III mainly falls into the three regions of Hpo, Hpo+Py and Hpo+Mpo (Fig. 8(d)). This indicates that most pyrrhotite of the Huangshaping deposit is hexagonal, and some of the Po III are monoclinic.

In recent years, the results of LA–ICP–MS analysis show that Co, Ni, Ti, Mn, As and Se are uniformly distributed in pyrrhotite by isomorphism or nanometer particles, and elements such as Cu,

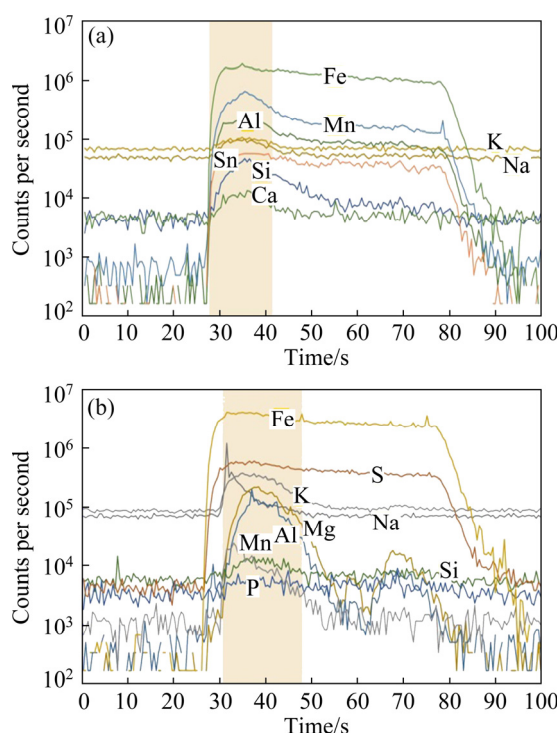


Fig. 9 Time-resolved analytical signals of LA-ICP-MS analyses: (a) Magnetite with inclusions; (b) Pyrrhotite with inclusions

Pb, Zn, Ti, V, Cr, Bi, Sn and W usually occur as fine mineral inclusions [50]. These inclusions are too small to be resolved by LA-ICP-MS and the elements in pyrrhotite from the Huangshaping deposit generally have a stable time-resolved LA-ICP-MS signal without any clear peaks or troughs that would indicate mineral inclusions. It is worth noting that some lithophile elements (K, Al, Na, Mg, and Si) show clear peaks in the time-resolved LA-ICP-MS signal, which can be considered as micro-silicate inclusions, as previously mentioned in magnetite (Fig. 9(b)). The pyrrhotite trace element composition in the Huangshaping deposit has a relatively small variation range (Table S3 of the supplementary materials).

The changes in the content of various elements in magnetite and pyrrhotite may record the chemical signature of the fluid composition, the fluid evolution, and the competition for elements between phases co-crystallizing with magnetite and pyrrhotite (e.g., base metal sulfides). Hence, the multielement characteristics of magnetite and pyrrhotite can be used as a good indicator of petrogenesis and mineralization.

5.2 Formation conditions of magnetite and pyrrhotite

The trace element content of magnetite and pyrrhotite has been demonstrated to be useful petrogenetic indicators due to their wide distribution in different deposit types [17,22,23,51]. Temperature, fluid composition, oxygen and sulfur fugacity, as well as buffering effects of the host rock are the main controlling factors for the magnetite composition. Previous studies have suggested that the partitioning of trace elements between magnetite and a hydrothermal fluid are controlled by the size of the cation site and the charge balance mechanism, followed by the nature of trace element in the hydrothermal fluid [10,52]. DING et al [9] compared magnetite compositions with different co-existing minerals (garnet, tremolite, and calcite) and found that spinel elements (Mg, Al, Ti, V, Zn, Mn, Ni, Co, Cr, Ga, Ge, and Sn) are unlikely affected by wall rock buffering, which means that the physicochemical conditions of the fluid can be reliably reflected by the major and trace elements of magnetite [53].

The understanding of the behavior of pyrrhotite during the evolution of hydrothermal fluid is of fundamental interest since the principal sulfide minerals (sphalerite, chalcopyrite, pyrite, and galena) almost ubiquitously occur to pyrrhotite. Pyrrhotite exhibits solid solutions between stoichiometric troilite (FeS) and Fe-deficient (sulfur excess) pyrrhotite, resulting in a chemical formula $Fe_{1-x}S$, where x denotes vacant octahedral sites [54]. Previous researches have demonstrated through a series of experiments that S and Fe atoms content can be used to quantify the temperature and sulfur fugacity during the re-equilibration crystallization of pyrrhotite [31,43,45,46].

5.2.1 Temperature estimation from trace element compositions

The low- and high-temperature minerals can potentially be distinguished by the content of Ti, V, Al, Mn and Ga [55,56]. Previous studies have suggested that the low-Ti content magnetite and Ti-rich oxides formed at low temperature and/or high $f(O_2)$, whereas Ti-rich magnetite formed at high temperature and/or relatively reducing conditions [57,58]. Exsolution lamellae and associated porosity are the important evidence to distinguish the high-temperature and low-temperature systems because exsolution is absent in

the latter system, which has a limited solubility of Ti [59].

The mineralization types and properties of hydrothermal fluids can be reflected in the trace elements of magnetite. In the (Al+Mn+Ca) vs (Ti+V) diagram (Fig. 10(a)), three generations of the magnetite observed plot in the skarn field, with relatively uniform Al+Mn+Ca but more distinct differences in Ti+V concentrations among the different generations. Similarly, in the Ni/Cr vs Ti scatter diagram, most of the magnetite data fall

in the hydrothermal area, and only individual data spots of Mag I are cast in the magmatic area (Fig. 10(b)). These further indicate that the Huangshaping is a skarn deposit that has evolved from magma and is related to granites. NADOLL et al [55] suggested that hydrothermal temperature is positively correlated with the Al+Mn and Ti+V content, whereas LIU et al [60] proposed that the lithophile elements like Al, Mn and Ca may not be suitable to determine the hydrothermal formation temperature because hydrothermal alteration could

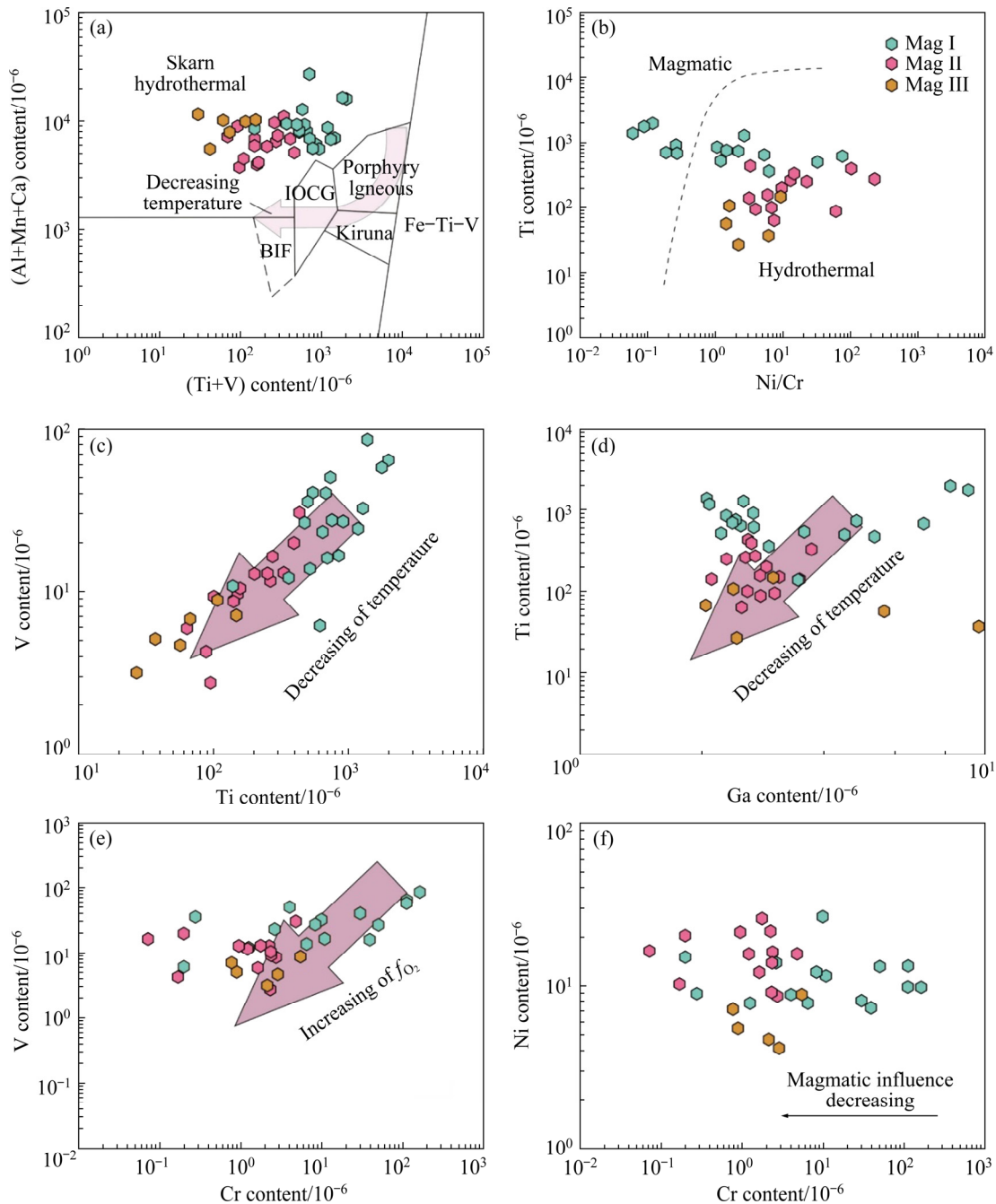


Fig. 10 Binary plots of selected trace elements from Huangshaping deposit: (a) (Al+Mn+Ca) vs (Ti+V) discrimination diagrams for magnetite (modified from Ref. [17]); (b) Ti vs Ni/Cr diagram (modified from Ref. [56]); (c) V vs Ti; (d) Ti vs Ga; (e) V vs Cr; (f) Ni vs Cr

affect the amount of silicate. The content of Al and Mn in magnetite at different stages remains relatively stable, while the content of Ti and V in different magnetite varies greatly. There are good correlations between Ti and V, Ga and Ti (Figs. 10(c, d)), and the content of Ti, V and Ga is the highest in Mag I, which indicates that the formation temperature of Mag I is the highest, and the temperature gradually decreases with the progress of crystallization process. Previous fluid inclusion temperature measurements of scheelite from the Huangshaping were 340–500 °C in the anhydrous skarn stage [60], with an average of 460 °C. This indicated that the crystallization temperature of magnetite (Mag I) formed in the early stage should be close to or lower than 460 °C, and the temperature of magnetite formed in the oxide stage (Mag II) and early quartz sulfide stage (Mag III) will be lower.

The final re-equilibration crystallization temperature between pyrrhotites can be estimated by the Fe molar fraction. The phase diagram model of equilibrium between pyrrhotite and pyrite solid solution at different temperatures was constructed through experiments (325–743 °C [44]; <(304±6) °C [45]; <350 °C [61]), and reveals the relationship between the re-equilibration crystallization temperature and the Fe molar fraction. The $T-x(\text{Fe})$ relationship follows an equation as follows:

$$T = -201.22x + 9854.32 \quad (1)$$

where T is the temperature, and x is the molar fraction of Fe [62].

Some abnormally high values in Po II and Po III were excluded because some of the pyrrhotite crystal types belonged to Mpo or had no co-crystallization with pyrite [43–46]. The results show that the crystallization temperatures of Po I range from 371.02 to 474.25 °C, with an average value of 420.46 °C, followed by 286.71 to 437.43 °C for Po II (average=380.45 °C), and 195.76 to 439.24 °C for Po III (average=341.81 °C), indicating that the different stage pyrrhotite formed in a high-temperature environment (Table S1 of the Supplementary Materials; Fig. 11(a)). This is supported by the temperature measurement results of fluid inclusions in the same mineralization stage (retrograde stage related to the W–Sn (Mo) ore body) (fluid inclusions temperature: 300–460 °C,

[63]). In contrast, the Pb–Zn mineralization associated with quartz porphyry shows fluid inclusion temperature from 135 to 307 °C, which is significantly lower than the fluid inclusion temperature (347 to 488 °C) of Pb–Zn ore bodies formed in the contact zone of granite porphyry [8].

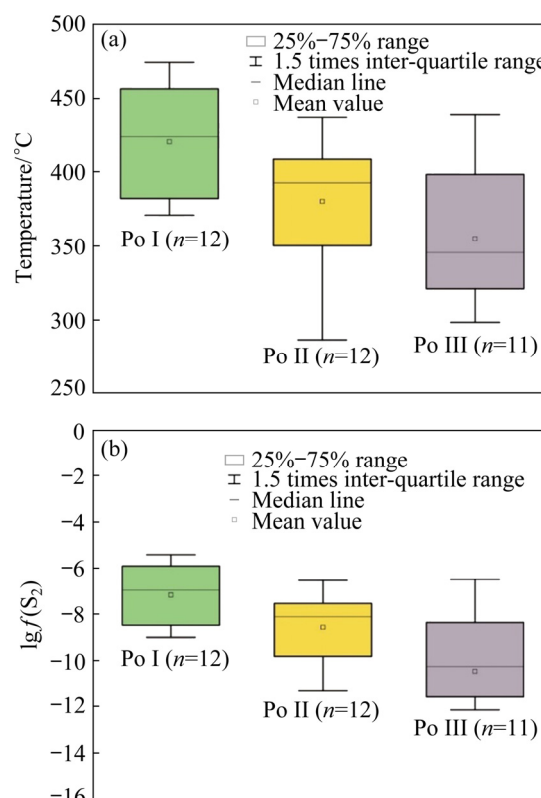


Fig. 11 Box chart of temperature calculated for different stages pyrrhotite (a), and for sulfur fugacity (b)

5.2.2 Redox environment

The oxidation state of vanadium in magnetite is usually used to estimate the relative oxygen fugacity prevalent during the evolution of ore-forming fluid [55,64]. Valence states of V include +3, +4, +5, where 4⁺ is the main valence state because the earth's oxygen fugacity is mainly in the range of iron-wustite (IW) +2 to iron-wustite +4 [65]. TOPLIS and CORGNE [66] suggested that V in magnetite decreases at high oxygen fugacity ($f_{\text{O}_2} = \text{IW} + 5$). V is positively correlated with Cr when V is +3, and V is positively correlated with Ti when V is +4 [67]. The three generations of magnetite from the Huangshaping deposit show a strong positive correlation between V and Ti, while only Mag I shows a weak positive correlation between V and Cr (Fig. 10(e)). This suggests that V³⁺ and V⁴⁺ co-exist in the anhydrous skarn stage and the high content of V in Mag I also indicates a relatively low

oxygen fugacity environment compared to Mag II and III. This phenomenon is consistent with the low oxygen fugacity, which suggested the decrease of Mo content in scheelite during the late prograde metamorphic stage in the Huangshaping deposit as proposed by DING et al [10]. The gradually decreasing content of V mainly with 4⁺ valence from Mag II to Mag III indicates that the oxygen fugacity increases gradually after entering the oxide stage. Chromium can also be used as an indicator of the change in oxygen fugacity. Cr is more mobile in the high valence state (6⁺) and is compatible with magnetite in the low valence state (3⁺) [68]. The lower Cr contents and higher Ni/Cr ratios of Mag II and III illustrate the higher oxygen fugacity (Figs. 10(b, e)), which is consistent with the change in oxygen fugacity reflected in the V content.

The content of Fe in pyrrhotite can not only be used to calculate the approximate temperature of mineral crystallization but can also be combined with the content of S to further estimate the sulfur fugacity of the fluid. TOULMIN and BARTON [69] obtained the following relationship of sulfur fugacity in the range of 743–320 °C through experimental calibration:

$$\lg f(S_2) = (70.03 - 85.83N_{\text{FeS}}) \left(\frac{1000}{T} - 1 \right) + 39.3 \times (1 - 0.998N_{\text{FeS}})^{1/2} - 11.91 \quad (2)$$

where $N_{\text{FeS}} = 2n(\text{Fe}) / (n(\text{Fe}) + n(\text{S}))$, where n is the mole number. MENGASON et al [70] further investigated the influence of Cu contents on the calculation of sulfur fugacity. The EPMA results of pyrrhotite in the Huangshaping deposit show that Cu content is very low, or below the detection limit (Table S3 of the Supplementary Materials). Consequently, we have used the equation by TOULMIN and BARTON [69] to calculate N_{FeS} . The sulfur fugacity ranges from -8.99 to -5.41 for Po I (average=-7.16), from -11.29 to -6.53 for Po II (average=-8.57), and from -18.81 to -6.48 for Po III (average=-10.46) based on the previous calculation of their respective re-equilibrium temperatures, indicating a process of decreasing sulfur fugacity during fluid evolution (Fig. 11(b)). ZHU et al [11] deduced that the sulfur fugacity decreased gradually during the W–Sn (Mo) crystallization of the high-temperature mineralizing process (0 to -15 for powellite and -10 to -30 for molybdenite).

5.2.3 Fluid–rock interaction

The granite porphyry and the limestone of the Shidengzi Formation are the main wall rocks of the W–Sn (Mo) ore body (Fig. 3). The formation and compositions of skarn minerals are due to the fluid–rock interaction [71]. The Ni content of magnetite is variable because Ni enters the lattice of magnetite and sulfide when these two minerals are co-crystallized [72]; however, this has little effect on the Co content. In the Huangshaping deposit, we observe from petrographic investigations that only Mag III coprecipitated with sulfides, which is also recognized in the lower Ni content in Mag III because some Ni partitions into the sulfide phase. In contrast, the Co and Ni contents of Mag I and Mag II are higher than those of Mag III since no competing sulfide mineral is co-crystallizing with magnetite (Fig. 6(b)). Cr content decreases from Mag I to Mag III (Figs. 10(b, f)), which is interpreted as decreasing magmatic fluid component influence and increasing hydrothermal influence (Fig. 10(f)).

The fluid–rock interaction may play an important role in producing the wide variation observed in Mo, and Sn contents [73]. The metasomatism associated with granite porphyry is suggested to lead to the elevated Mo and Sn contents in magnetite. It is reasonable to consider the high Sn and Mo contents in magnetite to be a result of skarnization. When magma upwelled into contact with the sedimentary rocks, it formed the earliest prograde alteration, mixing with the stratigraphic materials. During the progress of fluid–rock interactions, the increase of Sn and Mo elements and the decrease of lithophile elements can be considered as the enhancement of hydrothermal influence from Mag I to Mag II.

As mentioned earlier, tiny inclusions of silicate can be identified in both magnetite and pyrrhotite that could indicate intense fluid/wall rock interaction and incorporation of minerals in magnetite and pyrrhotite. According to this, changes in the content of elements in silicates in magnetite can be used as an indicator of fluid–rock interactions. Most of the lithophile elements (Na, Mg, Al, K) have the lowest content in Mag II, which was formed in the oxide stage. From Mag II to Mag III, the increase in the content of these elements may be due to the composition of the wall rock materials involved in the interaction.

Extensive fluid-rock interaction has been confirmed by the extremely high $^{87}\text{Sr}/^{86}\text{Sr}$ ratios (0.90396 to 1.51943) for the mineralized granite porphyry in the Huangshaping deposit [38]. In contrast, the uniform initial $^{87}\text{Sr}/^{86}\text{Sr}$ ratios (0.72894 to 0.83093) of the mineralized quartz porphyry, granophyre, and those of its unaltered counterpart indicate weak fluid metasomatism [4,35,38]. The fluid-rock interaction and wall rock assimilation process led to the formation of large-scale ore bodies around the granite porphyry.

5.3 Constraints on hydrothermal fluid evolution

The Huangshaping deposit is a representative polymetallic deposit related to the magma of deep origin in South China and was formed in an intra-continental extension environment [38]. At ~160 Ma, the granite porphyry slowly ascended to a depth of 4–5 km and reacted with the limestone of the Shidengzi Formation to form large-scale skarn [74]. The evolution of granite porphyry and the formation of W–Sn (Mo) ore bodies have been described in detail in previous studies [10,11,15,38,39,75]. These explained the evolution process and mechanism of granite porphyry and the high-temperature W–Sn (Mo) metallogenic system, while our work reveals the evolution process (compositions and properties) of hydrothermal fluid from the late anhydrous silicate stage to the late quartz–sulfide stage.

Based on the previous studies of skarn, the fluid amount in the magma system is increased because of the crystallization of anhydrous minerals (garnet and pyroxene), which resulted in the exsolution of Fe-bearing fluids and reaction in the contact zone of granite porphyry and the limestone of the Shidengzi Formation [35]. In the prograde stage, Mo-rich scheelite and abundant garnet co-precipitated, which represents the earliest precipitation of anhydrous silicate minerals [11]. As the fluid evolved to the hydrous silicate stage, the early crystallized minerals such as garnet underwent retrograde metamorphism and were transformed into actinolite, epidote, chlorite, and quartz. At the end of this stage, some magnetite (Mag I) was formed, after the high-temperature magmatic-hydrothermal system of W–Sn mineralization. In this high-temperature situation, some elements such as V, Ti, and Ga have the highest content in magnetite, and the content of V and the linear

relationship between V and Cr indicate a low oxygen fugacity environment. As the hydrothermal fluid evolved to the oxide stage, abundant Mo-poor scheelite, magnetite (Mag II), and minor molybdenite formed. With the progress of skarnization (decrease in temperature and increase in oxygen fugacity), the lithophile elements were consumed, resulting in the lowest content of Ca, K, Na, and Si in Mag II. Compared with the fluid from which Mag I crystallized, the oxygen fugacity of the fluid increased and precipitated Mag II with its characteristic trace element signature (Fig. 12) based on the high valence state of V (4^+) and the low content of Cr. The decrease in temperature and the increase in oxygen fugacity are the main reasons leading to the gradual precipitation of magnetite. The enhancement of the fluid-rock interaction accelerated the absorption of surrounding rock materials.

An important transformation occurred at the late oxide stage and the early quartz–sulfide stage. At this stage, the oxygen fugacity of the fluid was at its maximum, while the temperature decreased further. Hydrous silicate minerals, minor magnetite (Mag III), Cu- and Fe-sulfides (pyrite, Po I) were precipitated from the hydrothermal fluids. The increase in elements from silicate inclusions in magnetite indicates that at this stage fluid/wall rock interaction has increased (Figs. 6(a, b)). According to the quantitative calculation, the re-equilibrium temperature and sulfur fugacity of pyrrhotite are $420.46\text{ }^\circ\text{C}$ and -7.16 , respectively, equally indicating a high-temperature environment. From Po I to Po III, temperature and sulfur fugacity were constantly decreasing, in turn, minerals such as pyrite–arsenopyrite, and sphalerite crystallized. Most trace elements in pyrrhotite reached the highest concentrations at Po II (Fig. 6(c)), which crystallized during the main mineralization event for the sulfides (quartz–sulfide stage).

The complete fluid and mineral evolution were drawn in detail in Fig. 12. The overall process is that the hydrothermal system is going from post-magmatic conditions to cooler hydrothermal conditions, while the oxygen fugacity increases first, and then the sulfur fugacity decreases. This model characterizes the processes that occur after the evolution of prograde metamorphism, which is related to the high-temperature W–Sn metallogenic system associated with granite porphyry. This

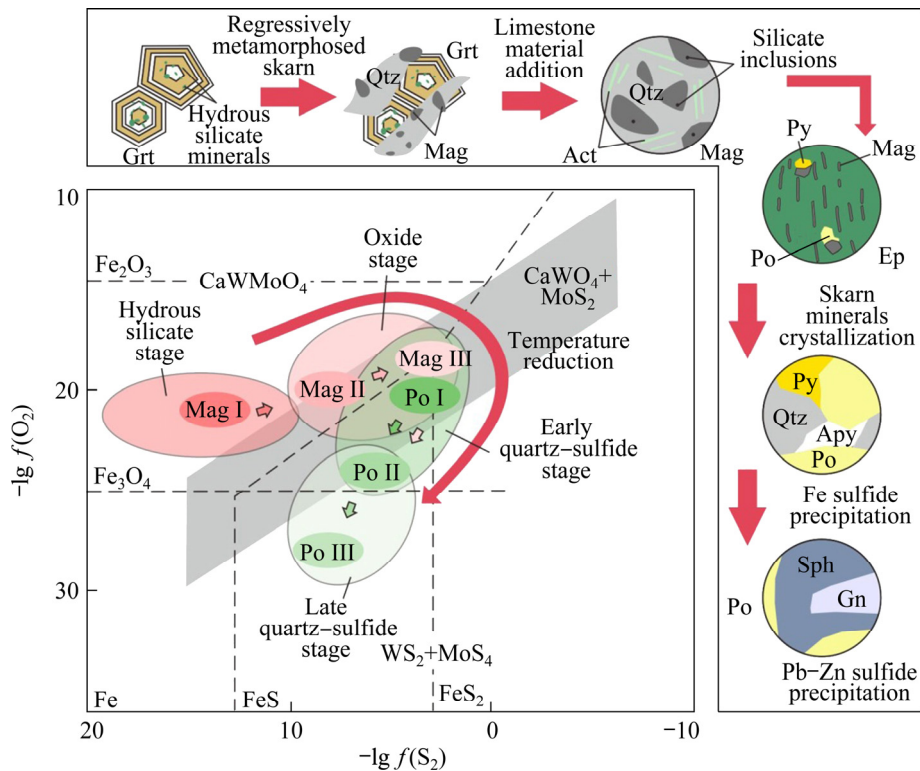


Fig. 12 Model illustrating fluid evolution and mineralization process during retrograde stage of high-temperature W–Sn metallogenic system in Huangshaping deposit, based on texture and chemical composition of magnetite and pyrrhotite (The $-\lg f(\text{S}_2)$ vs $-\lg f(\text{O}_2)$ diagram indicates the stability field of coexisting Fe-bearing minerals (modified from Hsu [76])

evolution model can be extended to some typical complex deposits in the Nanling Range, such as the Xitian W–Sn–Pb–Zn deposit, the Shizhuyuan W–Sn–Pb–Zn deposit, and the Jiepailing W–Sn–Pb–Zn deposit. Both skarn-type and vein-type ore bodies can be identified in these deposits, which are different in mineral assemblage and metallogenic type. Typically, in the Xitian deposit, skarn type mineralization occurs in the endo- and exo-contact zones between the Devonian limestone and the Yanshanian granite, while vein-type ore bodies are distributed in echelons and dip steeply towards the NE and strike S [34,77]. As a W–Sn–polymetallic deposit, Xitian may share a similar fluid evolution model with our work after the evolution of W–Sn mineralization. The strong evidence is that the redox environment changing of the Pb–Zn ore was from oxidizing to reducing [34] and the fluid inherited the high-temperature ore-forming conditions of W–Sn mineralization [78]. The homogenization temperature gradually decreases from 215–384 °C to 182–343 °C for W–Sn mineralization and Pb–Zn mineralization,

respectively [34]. In the Xitian ore field, the dominant cause of W–Sn precipitation is the fluid addition and fluid boiling, which caused the redox conditions to change to reduction, as evidenced by the large amounts of CH_4 in fluid inclusions [34], similar to the Xianghualing deposit [79]. The metallogenic model proposed in this work provides insight into the fluid evolution (temperature and redox environment) and mineralization, which can be extended to the Nanling polymetallic metallogenic belt.

6 Conclusions

(1) The Huangshaping deposit is characterized by different mineralization styles (skarn-type W–Sn (Mo), Pb–Zn, and vein-type Pb–Zn) associated with multiple granite intrusions (granite porphyry and quartz porphyry) and distinct metallogenic conditions. A complete metallogenic evolution of post-W–Sn mineralization, namely Pb–Zn skarn mineralization, has been determined in this study.

(2) Magnetite is widely developed in the

hydrous silicate stage (Mag I), the oxide stage (Mag II), and the early quartz–sulfide stage (Mag III). From Mag I to Mag III, the temperature was decreased, while the oxide fugacity was increased. During the transition from Mag II to Mag III, the content of silicate inclusions (characterized by Na, Al, Si, K, Ca) and some metallic elements (Mo, Sn, W, Pb) in magnetite increases due to the addition of wall rock materials. The influence of magmatic fluid is gradually weakened and the degree of water–rock interaction is gradually enhanced.

(3) Pyrrhotite was mainly developed in the early and late quartz–sulfide stage (Po I to Po III). The temperature and sulfur fugacity decreased gradually during this process. Most of the metallic elements are enriched first and then precipitated in the ore-bearing fluid, that is, they have the highest content in Po II.

Appendix

Appendix in this paper can be found at: <http://www.yxabcn.com/download/17-p3015-2021-0822-Appendix.pdf>

Acknowledgments

This work was supported by the National Key Research and Development Plan, China (No. 2018YFC0603901), and the National Natural Science Foundation of China (No. 41502067). Mr. ZHU was supported by the Fundamental Research Funds for the Central South University, China (No. 2021zzts0823). Many thanks go to Dr. Thomas ULRICH for his language editing on original manuscript.

References

- [1] LI Xian-hua, LI Wu-xian, LI Zheng-xiang. On the genetic classification and tectonic implications of the Early Yanshanian granitoids in the Nanling Range, South China [J]. Chinese Science Bulletin. 2007, 52(14): 1873–1885.
- [2] MAO Jin-wen, XIE Gui-qing, GUO Chun-li, CHUN Shu-chuan. Large-scale tungsten-tin mineralization in the Nanling region, South China: Metallogenic ages and corresponding geodynamic processes [J]. Acta Petrologica Sinica, 2007(10): 2329–2338. (in Chinese)
- [3] BAI Dao-yuan, HUANG Jian-zhong, LI Jin-dong, WANG Xian-hui, MA Tie-qiu, ZHANG Xiao-yang, CHEN Bi-he. Multiple geological elements constraint on the Mesozoic tectonic evolution of South China: apocalypse of the Mesozoic geological evolution in southeastern Hunan and the Hunan–Guangdong–Jiangxi border area [J]. Geotectonica et Metallogenia, 2007, 31(1): 1–13. (in Chinese)
- [4] HU Xin-lu, GONG Yong-jun, PI Dao-hui, ZHANG Zhen-jie, ZENG Guo-ping, XIONG Suo-fei, YAO Shun-zhen. Jurassic magmatism related Pb–Zn–W–Mo polymetallic mineralization in the central Nanling Range, South China: Geochronologic, geochemical, and isotopic evidence from the Huangshaping deposit [J]. Ore Geology Reviews, 2017, 91: 877–895.
- [5] KONG Hua, LI Hua, WU Qian-hogn, XI Xiao-shuang, DICK J M, GABO-RATIO J A S. Co-development of Jurassic I-type and A-type granites in southern Hunan, South China: dual control by plate subduction and intraplate mantle upwelling [J]. Geochemistry, 2018, 78(4): 500–520.
- [6] LI Huan, KONG Hua, ZHOU Zhe-kai, WU Qian-hong, XI Xiao-shuang, GABO-RATIO J A S. Ore-forming material sources of the Jurassic Cu–Pb–Zn mineralization in the Qin-Hang ore belt, South China: Constraints from S–Pb isotopes [J]. Geochemistry, 2019, 79(2): 280–306.
- [7] WU Jing-hua, LI Huan, ALGEO T J, JIANG Wei-cheng, ZHOU Zhe-kai. Genesis of the Xianghualing Sn–Pb–Zn deposit, South China: A multi-method zircon study [J]. Ore Geology Reviews, 2018, 102: 220–239.
- [8] LI Xiao-feng, HUANG Cheng, WANG Chun-zeng, WANG Li-fa. Genesis of the Huangshaping W–Mo–Cu–Pb–Zn polymetallic deposit in Southeastern Hunan Province, China: Constraints from fluid inclusions, trace elements, and isotopes [J]. Ore Geology Reviews, 2016, 79: 1–25.
- [9] DING T, MA D, LU J, ZHANG R. Garnet and scheelite as indicators of multi-stage tungsten mineralization in the Huangshaping deposit, southern Hunan Province, China [J]. Ore Geology Reviews, 2018, 94: 193–211.
- [10] DING Teng, MA Dong-sheng, LU Jian-jun, ZHANG Rong-qing. Magnetite as an indicator of mixed sources for W–Mo–Pb–Zn mineralization in the Huangshaping polymetallic deposit, southern Hunan Province, China [J]. Ore Geology Reviews, 2018, 95: 65–78.
- [11] ZHU Da-peng, LI Huan, ALGEO T J, JIANG Wei-cheng, WANG Chong. The prograde-to-retrograde evolution of the Huangshaping skarn deposit (Nanling Range, South China) [J]. Mineralium Deposita, 2021, 56(6): 1087–1110.
- [12] LEI Zhe-heng, CHEN Fu-wen, CHEN Zheng-hui, XU Yi-ming, GONG Shu-qing, LI Hua-qin, MEI Yu-ping, QU Wen-jun, WANG Deng-hong. Petrogenetic and metallogenic age determination of the Huangshaping lead–zinc polymetallic deposit and its geological significance [J]. Acta Geoscientia Sinica, 2010, 31(4): 532–540.
- [13] JIANG Wei-cheng, LI Huan, TURNER S, ZHU Da-peng, WANG Chong. Timing and origin of multi-stage magmatism and related W–Mo–Pb–Zn–Fe–Cu mineralization in the Huangshaping deposit, South China: An integrated zircon study [J]. Chemical Geology, 2020, 552: 119782.
- [14] MA Li-yan, LU Yuan-fa, QU Wen-jun, FU Jian-ming. Re–Os isotopic chronology of molybdenites in Huangshaping lead-zinc deposit, southeast Hunan, and its geological implications [J]. Mineral Deposits, 2007, 26(4): 425. (in Chinese)
- [15] LI Huan, YONEZU K, WATANABE K, TINDELL T. Fluid origin and migration of the Huangshaping W–Mo polymetallic deposit, South China: Geochemistry and ⁴⁰Ar/³⁹Ar geochronology of hydrothermal K-feldspars [J]. Ore Geology Reviews, 2017, 86: 117–129.

- [16] CHUNG D, ZHOU Mei-fu, GAO Jian-feng, CHEN W T. In-situ LA-ICP-MS trace elemental analyses of magnetite: The late Palaeoproterozoic Sokoman Iron Formation in the Labrador Trough, Canada [J]. *Ore Geology Reviews*, 2015, 65: 917–928.
- [17] DUPUIS C, BEAUDOIN G. Discriminant diagrams for iron oxide trace element fingerprinting of mineral deposit types [J]. *Mineralium Deposita*, 2011, 46(4): 319–335.
- [18] HUANG Jin-chuan, PENG Jian-tang, YANG Jie-hua, ZHANG Bang-lu, XU Chun-xia. Precise zircon U–Pb and molybdenite Re–Os dating of the Shuikoushan granodiorite-related Pb–Zn mineralization, southern Hunan, South China [J]. *Ore Geology Reviews*, 2015, 71: 305–317.
- [19] LIU Ping-ping, ZHOU Mei-fu, CHEN W T, GAO Jian-feng, HUANG Xiao-wen. In-situ LA-ICP-MS trace elemental analyses of magnetite: Fe–Ti–(V) oxide-bearing mafic-ultramafic layered intrusions of the Emeishan Large Igneous Province, SW China [J]. *Ore Geology Reviews*, 2015, 65: 853–871.
- [20] NADOLL P, MAUK J L, LEVEILLE R A, KOENIG A E. Geochemistry of magnetite from porphyry Cu and skarn deposits in the southwestern United States [J]. *Mineralium Deposita*, 2015, 50(4): 493–515.
- [21] MCQUEEN K G, CROSS A J, EGGLETON R A. Magnetite as a geochemical sampling medium: Application to skarn deposits [M]. Brisbane: Geological Society of Australia, 1998: 194–199.
- [22] CONN C D, SPRY P G, LAYTON-MATTHEWS D, VOINOT A, KOENIG A. The effects of amphibolite facies metamorphism on the trace element composition of pyrite and pyrrhotite in the Cambrian Nairne Pyrite Member, Kanmantoo Group, South Australia [J]. *Ore Geology Reviews*, 2019, 114: 103128.
- [23] MANSUR E T, BARNES S J, DURAN C J. An overview of chalcophile element content of pyrrhotite, pentlandite, chalcopyrite, and pyrite from magmatic Ni–Cu–PGE sulfide deposits [J]. *Mineralium Deposita*, 2021, 56(1): 179–204.
- [24] MANSUR E T, BARNES S, DURAN C J, SLUZHENIKIN S F. Distribution of chalcophile and platinum-group elements among pyrrhotite, pentlandite, chalcopyrite and cubanite from the Noril's k-Talnakh ores: Implications for the formation of platinum-group minerals [J]. *Mineralium Deposita*, 2020, 55(6): 1215–1232.
- [25] CIOBANU C L, COOK N J, UTSUNOMIYA S, KOGAGWA M, GREEN L, GILBERT S, WADE B. Gold-telluride nanoparticles revealed in arsenic-free pyrite [J]. *American Mineralogist*, 2012, 97(8/9): 1515–1518.
- [26] COOK N, CIOBANU C, GEORGE L, ZHU Z Y, WADE B, EHRIG K. Trace element analysis of minerals in magmatic-hydrothermal ores by laser ablation inductively-coupled plasma mass spectrometry: Approaches and opportunities [J]. *Minerals*, 2016, 6(4): 111.
- [27] LI Xian-hua, MCCULLOCH M T. Secular variation in the Nd isotopic composition of Neoproterozoic sediments from the southern margin of the Yangtze Block: Evidence for a Proterozoic continental collision in Southeast China [J]. *Precambrian Research*, 1996, 76(1/2): 67–76.
- [28] WANG Yue-jun, FAN Wei-ming, SUN Min, LIANG Xin-quan, ZHANG Yuan-fa, PENG Tou-ping. Geochemical and geothermal constraints on petrogenesis of the Indosinian peraluminous granites in the South China Block: A case study in the Hunan Province [J]. *Lithos*, 2007, 96(3/4): 475–502.
- [29] XU Xi-sheng, O'REILLY S Y, GRIFFIN W L, WANG Xiao-lei, PEARSON N J, HE Zhen-yu. The crust of Cathaysia: Age, assembly and reworking of two terranes [J]. *Precambrian Research*, 2007, 158(1/2): 51–78.
- [30] LI Zheng-xiang, LI Xian-hua. Formation of the 1300-km-wide intracontinental orogen and postorogenic magmatic Province in Mesozoic South China: A flat-slab subduction model [J]. *Geology*, 2007, 35(2): 179–182.
- [31] LI Xian-hua, SASAKI M. Hydrothermal alteration and mineralization of Middle Jurassic Dexing porphyry Cu–Mo deposit, southeast China [J]. *Resource Geology*, 2007, 57(4): 409–426.
- [32] LI Xiao-feng, WATANABE Y, YI Xian-kui. Ages and sources of ore-related porphyries at Yongping Cu–Mo deposit in Jiangxi Province, southeast China [J]. *Resource Geology*, 2013, 63(3): 288–312.
- [33] LEGROS H, RICHARD A, TARANTOLA A, KOUZMANOV K, MERCADIER J, VENNEMANN T, MARIGNAC C, CUNEY M, WANG R C, CHARLES N, BAILLY L, LESPINASSE M Y. Multiple fluids involved in granite-related W–Sn deposits from the world-class Jiangxi Province (China) [J]. *Chemical Geology*, 2019, 508: 92–115.
- [34] LIU Biao, WU Qian-hong, LI Hua, WU Jin-hua, CAO Jin-ya, JIANG Jiang-bo, LIANG Wei. Fault-controlled fluid evolution in the Xitian W–Sn–Pb–Zn–fluorite mineralization system (South China): Insights from fluorite texture, geochemistry and geochronology [J]. *Ore Geology Reviews*, 2020, 116: 103233.
- [35] DING Teng, MA Dong-sheng, LU Jian-jun, ZHANG Rong-qing, ZHANG Si-tao. S, Pb, and Sr isotope geochemistry and genesis of Pb–Zn mineralization in the Huangshaping polymetallic ore deposit of southern Hunan Province, China [J]. *Ore Geology Reviews*, 2016, 77: 117–132.
- [36] ZHU Xin-you, WANG Jing-bin, WANG Yan-li, CHENG Xi-yin, FU Qi-bin. Sulfur and lead isotope constraints on ore formation of the Huangshaping W–Mo–Bi–Pb–Zn polymetallic ore deposit, Hunan Province, South China [J]. *Acta Perologica Sinica*, 2012, 28(12): 3798–3808. (in Chinese)
- [37] ZHAO Lian-jie, ZHANG Yu, SHAO Yong-jun, LI Hong-bin, SAJJAD A S, ZHOU Wei-jian. Using garnet geochemistry discriminating different skarn mineralization systems: Perspective from Huangshaping W–Mo–Sn–Cu polymetallic deposit, South China [J]. *Ore Geology Reviews*, 2021, 138: 104412.
- [38] LI Huan, PALINKAŠ L A, EVANS N J, WATANABE K. Genesis of the Huangshaping W–Mo–Cu–Pb–Zn deposit, South China: Role of magmatic water, metasomatized fluids, and basinal brines during intra-continental extension [J]. *Geological Journal*, 2020, 55(2): 1409–1430.
- [39] DING Teng, WANG Jia, TAN Ting-ting, MA Dong-sheng, LU Jian-jun, ZHANG Rong-qing, LIANG Jin, ZHU Chuan-wei, WU Bin. Accumulation of sulfides in the basement of southern Hunan Province, China: Implications for Pb–Zn

- mineralization related to reduced granitoids [J]. *Ore Geology Reviews*, 2021, 129: 103939.
- [40] HU Zhao-chu, GAO Shan, LIU Yong-sheng, HU Sheng-dong, CHEN Hai-hong, YUAN Hong-lin. Signal enhancement in laser ablation ICP-MS by addition of nitrogen in the central channel gas [J]. *Journal of Analytical Atomic Spectrometry*, 2008, 23(8): 1093–1101.
- [41] HU Zhao-chu, LIU Yong-sheng, GAO Shan, XIAO Shao-quan, ZHAO Lai-shi, GÜNTHER D, LI Ming, ZHANG Wen, ZONG Ke-qing. A “wire” signal smoothing device for laser ablation inductively coupled plasma mass spectrometry analysis [J]. *Spectrochimica Acta Part B: Atomic Spectroscopy*, 2012, 78: 50–57.
- [42] LIU Yong-sheng, HU Zhao-chu, GAO Shan, GÜNTHER D, XU Juan, GAO Chang-gui, CHEN Hai-hong. In situ analysis of major and trace elements of anhydrous minerals by LA-ICP-MS without applying an internal standard [J]. *Chemical Geology*, 2008, 257(1/2): 34–43.
- [43] DESBOROUGH G A, CARPENTER R H. Phase relations of pyrrhotite [J]. *Economic Geology*, 1965, 60(7): 1431–1450.
- [44] ARNOLD R G. Equilibrium relations between pyrrhotite and pyrite from 325 degrees to 743 degrees C [J]. *Economic Geology*, 1962, 57(1): 72–90.
- [45] ARNOLD R G. Pyrrhotite phase relation below 304 [J]. *Economic Geology*, 1969, 64(4): 405–419.
- [46] KISSIN S A, SCOTT S D. Phase relations involving pyrrhotite below 350 degrees C [J]. *Economic Geology*, 1982, 77(7): 1739–1754.
- [47] DEDITIUS A P, REICH M, SIMON A C, SUVOROVA A, KNIPPING J, ROBERTS M P, RUBANOV S, DODD A, SAUNDERS M. Nanogeochemistry of hydrothermal magnetite [J]. *Contributions to Mineralogy and Petrology*, 2018, 173(6): 1–20.
- [48] WECHSLER B A, LINDSLEY D H, PREWITT C T. Crystal structure and cation distribution in titanomagnetites ($\text{Fe}_{3-x}\text{Ti}_x\text{O}_4$) [J]. *American Mineralogist*, 1984, 69(7/8): 754–770.
- [49] ZHAO W W, ZHOU M F. In-situ LA-ICP-MS trace elemental analyses of magnetite: The Mesozoic Tengtie skarn Fe deposit in the Nanling Range, South China [J]. *Ore Geology Reviews*, 2015, 65: 872–883.
- [50] LARGE R R, MASLENNIKOV V V, ROBERT F, DANYUSHEVSKY L V, CHANG Z. Multistage sedimentary and metamorphic origin of pyrite and gold in the giant Sukhoi Log deposit, Lena gold province, Russia [J]. *Economic Geology*, 2007, 102(7): 1233–1267.
- [51] NADOLL P, MAUK J L, HAYES T S, KOENIG A E, BOX S E. Geochemistry of magnetite from hydrothermal ore deposits and host rocks of the Mesoproterozoic Belt Supergroup, United States [J]. *Economic Geology*, 2012, 107(6): 1275–1292.
- [52] GHADERI M, PALIN J M, CAMPBELL I H, SYLVESTER P J. Rare earth element systematics in scheelite from hydrothermal gold deposits in the Kalgoorlie-Norseman region, Western Australia [J]. *Economic Geology*, 1999, 94(3): 423–437.
- [53] SUN Zhi-yuan, WANG Jing-bin, WANG Yu-wang, LONG Ling-li. Zircon and garnet U-Pb dating and in situ trace element of magnetite from the Hongyuntan Fe deposit, Eastern Tianshan, NW China [J]. *Ore Geology Reviews*, 2020, 127: 103813.
- [54] FLEET M E. Phase equilibria at high temperatures [J]. *Reviews in Mineralogy and Geochemistry*, 2006, 61(1): 365–419.
- [55] NADOLL P, ANGERER T, MAUK J L, FRENCH D, WALSH J. The chemistry of hydrothermal magnetite: A review [J]. *Ore Geology Reviews*, 2014, 61: 1–32.
- [56] DARE A S, BARNES S J, BEAUDOIN G, MÉRIC J, BOUTROY E, POTVIN-DOUCET C. Trace elements in magnetite as petrogenetic indicators [J]. *Mineralium Deposita*, 2014, 49(7): 785–796.
- [57] CHEN Wei, YING Yuan-can, BAI Tian, ZHANG Jin-jun, JIANG Shao-yong, ZHAO Kui-dong, SHIN D, KYNICKY J. In situ major and trace element analysis of magnetite from carbonatite-related complexes: Implications for petrogenesis and ore genesis [J]. *Ore Geology Reviews*, 2019, 107: 30–40.
- [58] HEMLEY J J, CYGAN G L, FEIN J B, ROBINSON G R, D'ANGELO W M. Hydrothermal ore-forming processes in the light of studies in rock-buffered systems; I, Iron-copper-zinc-lead sulfide solubility relations [J]. *Economic Geology*, 1992, 87(1): 1–22.
- [59] MENG Xiang-jin, HOU Zeng-qian, DONG Guang-yu, LIU Jian-guang, ZOU Li-yan, YANG Zhu-sheng, XIAO Mao-zhang. Geological characteristics and mineralization timing of the Lengshuikeng porphyry Pb–Zn–Ag deposit, Jiangxi Province [J]. *Acta Geologica Sinica*. 2009, 83(12): 1951–1967. (in Chinese)
- [60] LIU Yi-nan, FAN Yu, ZHOU Tao-fa, WHITE N C, HONG Hao-lan, ZHANG Wei, ZHANG Le-jun. In-situ LA-ICP-MS trace element analysis of magnetite from Mesozoic iron oxide apatite (IOA) deposits in the Luzong volcanic basin, Eastern China [J]. *Journal of Asian Earth Sciences*. 2018, 166: 233–246.
- [61] BARKER W W, PARKS T C. The thermodynamic properties of pyrrhotite and pyrite: A re-evaluation [J]. *Geochimica et Cosmochimica Acta*, 1986, 50(10): 2185–2194.
- [62] ZHANG Shu-geng, SHI De-feng, HAN Shi-li, LI Gui-xiu. Genetic mineralogical study of pyrrhotite in the Dingjiashan Pn–Zn ore district, Fujian Province [J]. *Journal of Mineralogy and Petrology*. 2011, 31(3): 11–17.
- [63] HUANG Cheng, LI Xiao-feng, WANG Li-fa, LIU Feng-ping. Fluid inclusion study of the Huangshaping polymetallic deposit, Hunan Province, South China [J]. *Acta Petrologica Sinica*. 2013, 29(12): 4232–4244. (in Chinese)
- [64] ACOSTA-GÓNGORA P, GLEESON S A, SAMSON I M, OOTES L, CORRIVEAU L. Trace element geochemistry of magnetite and its relationship to Cu–Bi–Co–Au–Ag–U–W mineralization in the great bear magmatic zone, NWT, Canada* [J]. *Economic Geology*, 2014, 109: 1901–1928.
- [65] PAPIKE J J, KARNER J M, SHEARER C K. Comparative planetary mineralogy: Valence state partitioning of Cr, Fe, Ti, and V among crystallographic sites in olivine, pyroxene, and spinel from planetary basalts [J]. *American Mineralogist*, 2005, 90(2/3): 277–290.
- [66] TOPLIS M J, CORGNE A. An experimental study of element partitioning between magnetite, clinopyroxene and iron-bearing silicate liquids with particular emphasis on

- vanadium [J]. Contributions to Mineralogy and Petrology, 2002, 144(1): 22–37.
- [67] PAPIKE J J, KARNER J M, SHEARER C K. Comparative planetary mineralogy: V/(Cr+ Al) systematics in chromite as an indicator of relative oxygen fugacity [J]. American Mineralogist, 2004, 89(10): 1557–1560.
- [68] JAMES B. Chromium [M]//Encyclopedia of environmental management. Boca Raton: CRC Press, 2015: 77–82.
- [69] TOULMIN P III, BARTON P B Jr. A thermodynamic study of pyrite and pyrrhotite [J]. Geochimica et Cosmochimica Acta, 1964, 28(5): 641–671.
- [70] MENGASON M J, PICCOLI P M, CANDELA P. Synsedimentary, diagenetic, and metamorphic pyrite, pyrrhotite, and marcasite at the Homestake BIF-hosted gold deposit, synsedimentary, diagenetic, and metamorphic pyrite, pyrrhotite, and marcasite at the Homestake BIF-hosted gold deposit [J]. Economic Geology, 2010, 105(6): 1163–1169.
- [71] MEINERT L D, HEDENQUIST J W, SATOH H, MATSUHISA Y. Formation of anhydrous and hydrous skarn in Cu–Au ore deposits by magmatic fluids [J]. Economic Geology, 2003, 98(1): 147–156.
- [72] DARE S A S, BARNES S J, BEAUDOIN G. Variation in trace element content of magnetite crystallized from a fractionating sulfide liquid, Sudbury, Canada: Implications for provenance discrimination [J]. Geochimica et Cosmochimica Acta, 2012, 88: 27–50.
- [73] QI You-qiang, HU Rui-zhong, GAO Jian-feng, GAO Wei, GONG Hao-tian. Trace element characteristics of magnetite: Constraints on the genesis of the Lengshuikeng Ag–Pb–Zn deposit, China [J]. Ore Geology Reviews, 2021, 129: 103943.
- [74] LI Huan, PALINKAS L A, WATANABE K, XI Xiao-shuang. Petrogenesis of Jurassic A-type granites associated with Cu–Mo and W–Sn deposits in the central Nanling region, South China: Relation to mantle upwelling and intra-continental extension [J]. Ore Geology Reviews, 2018, 92: 449–462.
- [75] LI Huan, WATANABE K, YONEZU K. Zircon morphology, geochronology and trace element geochemistry of the granites from the Huangshaping polymetallic deposit, South China: Implications for the magmatic evolution and mineralization processes [J]. Ore Geology Reviews, 2014, 60: 14–35.
- [76] HSU L C. Effects of oxygen and sulfur fugacities on the scheelite-tungstenite and powellite-molybdenite stability relations [J]. Economic Geology, 1977, 72(4): 664–670.
- [77] XIONG Yi-qu, SHAO Yong-jun, ZHOU Hao-di, WU Qian-hong, LIU Jina-ping, WEI Han-tao, ZHAO Rui-cheng, CAO Jing-ya. Ore-forming mechanism of quartz-vein-type W–Sn deposits of the Xitian district in SE China: Implications from the trace element analysis of wolframite and investigation of fluid inclusions [J]. Ore Geology Reviews, 2017, 83: 152–173.
- [78] CAO Jing-ya, YANG Xiao-yong, DU Jian-guo, WU Qian-hong, KONG Hua, LI Huan, WAN Qiu, XI Xiao-shuang, GONG Yu-shuang, ZHAO Hua-rong. Formation and geodynamic implication of the Early Yanshanian granites associated with W–Sn mineralization in the Nanling range, South China: An overview [J]. International Geology Review, 2018, 60(11/12/13/14): 1744–1771.
- [79] ZHENG Xu, LIU Jian-ping, CHEN Wei-kang, SAHO Yong-jun, TIAN Xu-feng, WEN Yi-zhuo, LIU Shao-qing, DING Tao. Characteristics and genesis of in mineralization of stratoid polymetallic orebodies hosted by clastic rock in Xianghualing ore field, South Hunan [J]. The Chinese Journal of Nonferrous, 2022, doi: <http://kns.cnki.net/kcms/detail/43.1238.TG.20210818.0930.001.html>. (in Chinese)

南岭黄沙坪矽卡岩矿床花岗斑岩铅锌矿化成矿环境特征

朱大鹏¹, 李欢¹, 蒋维诚², 王冲¹, 胡晓君¹, 孔华¹

1. 中南大学 地球科学与信息物理学院 有色金属成矿预测与地质环境监测教育部重点实验室, 长沙 410083;

2. Department of Earth and Environmental Sciences, Macquarie University, NSW, 2109, Australia

摘要: 黄沙坪多金属矿床位于南岭地区, 矿床内发育大量的与浅成花岗岩有关的块状矽卡岩型和脉型多金属矿化。为了更好地约束矽卡岩的形成和成矿过程, 对含水硅酸盐阶段、氧化物阶段、早期石英–硫化物阶段和晚期石英–硫化物阶段的磁铁矿和磁黄铁矿进行矿物组合、结构构造和地球化学特征研究。利用电子探针(EPMA)和激光剥蚀电感耦合等离子质谱(LA–ICP–MS)对磁铁矿和磁黄铁矿的地球化学组成进行分析。结果表明, 磁铁矿中可能存在的硅酸盐包裹体指示矿化过程有围岩的参与作用。磁黄铁矿中元素地球化学趋势显示灰岩对磁黄铁矿结晶过程的影响。PoI、PoII 和 PoIII 的再平衡温度分别为 420.46、380.45 和 341.81 °C, 表明该成矿过程是在延续高温 W–Sn 成矿矿化系统之后连续演化。磁铁矿中 Ni 和 V 含量的变化反映从 Mag I 到 Mag III 的氧逸度逐渐降低, 根据磁黄铁矿元素含量计算出的硫逸度也指示一个硫逸度逐渐降低的过程。这种连续的矽卡岩成矿演化过程有助于更好地了解黄沙坪矿床退变质阶段成矿环境的变化。

关键词: 微量元素; 磁铁矿; 磁黄铁矿; 地球化学

(Edited by Xiang-qun LI)